Strain-rate-dependent mechanics and impact performance of epoxy-based nanocomposites

Mertol Tüfekci [a], Burak Özkal [b], Chris Maharaj [c], Haibao Liu [d,*], John P. Dear [a,*], Loïc Salles [a]

[a] Department of Mechanical Engineering, Imperial College London, London, SW7 2AZ, UK
[b] Department of Metallurgical and Materials Engineering, Istanbul Technical University, Istanbul, 34469, Turkey
[c] Department of Mechanical and Manufacturing Engineering, The University of the West Indies, St. Augustine, Republic of Trinidad and Tobago
[d] Centre for Aeronautics, Cranfield University, Cranfield, MK43 0AL, UK

ARTICLE INFO

Keywords:
Nanocomposites
Mechanical characterisation
Nonlinear behaviour
Strain-rate-dependence
Numerical simulation

ABSTRACT

Strain-rate-dependent mechanical properties and impact performance of manufactured epoxy-based nanocomposites are investigated. As reinforcements, fumed silica (FS) and halloysite nanotube (HNT) are used alongside Albipox 1000 and Nanopox F700. First, the internal structures of the composites are visualised using scanning electron microscopy (SEM). To identify the strain-rate-dependent mechanical properties, three-point bend tests are conducted at three different strain rate levels. For the impact resistance, Charpy impact tests are performed. For further investigations of the mechanical properties of the composites, mean-field homogenisation (MFH) and finite element (FE) analyses on the representative volume elements (RVE) are performed for each type of composite material. Overall, the modelling and experiments are in good agreement and account for the mechanical behaviour of these epoxy-based nanocomposites.

1. Introduction

Nonlinearity can arise in homogeneous materials and nonhomogeneous materials like composites, particularly when subjected to large deformations [1]. One way of categorising the materials in engineering is based on how they are deformed when loaded. The deformation is expressed as a function of load, which directly makes the distinction of the materials being linear or nonlinear. Thus, if the stiffness of the material is constant, then the material characteristics are linear, whereas if the stiffness varies for the different stages of deformation and the deformation rates, then the material has a nonlinear manner [2]. In many cases with polymers, a linear relation does not accurately represent the behaviour of such material. For example, the nonlinear deformation of polymers can be affected by the presence of reinforcement [3].

The nonlinearities based on material characteristics can be expressed mathematically within the constitutive equation of the materials [4,5]. Thus, there are different material models in the literature that have been used by researchers over the decades. Material models differ by functions used in the constitutive equations. These functions are generally based on experimental results of material characterisation focusing on mechanical behaviour under various loading conditions [6]. Since polymers are usually more compliant materials with more damping capacity than other engineering materials such as metals and ceramics, a different material model is required to represent their behaviour. The material modelling method, which includes the damping and/or strain-rate-dependent behaviour, is called viscoelasticity which describes the material behaviour as a combination of viscous and elastic. Due to the viscous behaviour, this modelling method adds damping and the strain-rate-dependency to the material characteristics [7–9]. This damping/strain-rate-dependence can be represented in various forms such as linear viscoelasticity, nonlinear viscoelasticity and fractional derivatives.

Polymer-based composites are known to have complicated characteristics, especially those with nanoreinforcements [10–14]. The major difference between conventional composites and nanocomposites is caused by the great surface area/volume ratio of the nanoreinforcements, which leads to larger interphase regions that tend to have a nonlinear characteristic [15–17]. The resultant behaviour can be even more complicated in the presence of multiple nanoreinforcements [18–21]. Halloysite nanotubes (HNT), carbon nanotubes (CNT), fumed silica (FS), silica, and rubber nanoparticles are among the most common particles for the fabrication of nanocomposites [3,22–26]. Experiments are preferred to be able to characterise the behaviour of composites, and when performed are often found to be more reliable [27]. There are several methods to experimentally characterise the nonlinear dynamic behaviour. Kliem et al. use a vibration test setup to explore the dynamics of a cylindrical composite structure [28]. Xu and Gupta use dynamic

mechanical analysis (DMA) and they develop a method to extract the storage modulus for various strain rates and temperatures [29]. Xu et al. again use DMA to characterise the elastic behaviour of nanocomposites at a range of strain rates and temperatures [30]. Esmaeeli et al. propose a new setup to measure the mechanical properties at high frequencies [31]. Pierro and Carbone also design a vibrational test setup using an impact hammer to extract the mechanical properties, which are then compared with the results obtained from DMA [32].

There are studies that use the data acquired from the virtual experiments performed using their material models [33]. However, the mechanisms that control and shape that complicated mechanical behaviour are often difficult to interpret. It is thought that the internal structure of the material is among the most important parameters that control the mechanics of such composites. Several theories, such as molecular dynamics and nonlocal continuum theory, explore the mechanics on small scales [4,17,34–36]. Therefore, multiscale modelling approaches are developed to investigate the small-scale structures' effective mechanics, such as nanocomposites [33,37]. Mori–Tanaka mean-field homogenisation (MFH) is among the most common and convenient methods of multiscale modelling [38]. It is proven to work well with particulate reinforced nanocomposites [6,39]. The finite element method (FEM) is another numerical modelling approach that can be used to perform multiscale analyses on nanocomposites. The stress analysis is conducted by generating representative volumetric elements (RVE) of the nanocomposites and applying periodic boundary conditions (PBC) to the generated elements, and then the effective mechanical properties of the materials can be computed [40–44]. Compared to Mori–Tanaka or any other MFH methods, the FE model usually produces more accurate results. However, its computational cost is also greater [45,46].

This study conducts detailed investigations of strain-rate-dependent mechanics and impact resistance of nanocomposites. Epoxy-based nanocomposites are manufactured with four different reinforcements, FS, HNT, silica (Nanopox F700) and rubber (Albipox 1000), as well as the control samples made of unreinforced epoxy. To explore the synergistic behaviour of the reinforcements, FS and HNT are also combined together in equal masses. Silica and rubber are put together for the same purpose. To minimise the effects of manufacturing processes on the mechanics of the nanocomposites, a consistent manufacturing process is designed and employed for all sorts of materials. To ensure that there are no substantial irregularities in the material, scanning electron microscopy (SEM) is used to view the interior structure of the manufactured materials. Afterwards, strain-rate-dependent mechanical properties are experimentally characterised with three-point bend tests at three different strain rates. Charpy impact tests are conducted to explore the impact resistance. To be able to interpret the results of the experimental procedures further, numerical simulations (Mori–Tanaka MFH and FE) are developed to characterise the mechanics of the composites prepared. These numerical simulations (Mori–Tanaka MFH and FE) both analyse RVEs with appropriately shaped inclusions. Thus, the main contribution of this study is to observe experimentally the effects of the mentioned nanoreinforcements on the epoxy-based composites. Furthermore, the mechanisms that change the mechanical properties of the composites are revealed through numerical analysis.

2. Material preparation and experimentation

To conduct this part of the study, epoxy and epoxy-based composite samples are manufactured. A scanning electron microscope (SEM) is used to examine the interior structures of these manufactured composite samples, which primarily determine the mechanical characteristics of those materials. The composites are also put through three-point bend tests at different deformation speeds to characterise the strain-rate-dependence of their mechanical properties. Finally, Charpy impact tests are performed to get an understanding of how ductility is affected by the reinforcements. In this section, manufacturing and testing procedures are described in detail.

Table 1
Composition in mass of material depending on the nanoparticle reinforcements (mass is measured in g.).

Mass fractions (m_f)	Matrix mass [g]		Reinforcement mass [g]		
	Epoxy resin	Hardener	FS	HNT	FS and HNT
0.005	255.86	102.34	1.80	1.80	1.80
0.01	254.57	101.83	3.60	3.60	3.60
0.015	253.29	101.31	5.40	5.40	5.40
0.02	252.00	100.80	7.20	7.20	7.20

2.1. Material preparation and manufacturing process of the samples

In terms of material groups, first epoxy samples are manufactured to be used as a benchmark to display the effects of the reinforcing materials on the mechanics of the nanocomposites. Epoxy resin MGS@ L 285 by Hexion is chosen along with the hardener MGS@ 285 by Hexion. Then, FS Aerosil 200 by Evonik, HNT by Nanografi and their equal mass combinations are used to reinforce the epoxy matrix. For this material group, the reinforcements are added to the resin by 0.5%, 1%, 1.5% and 2% in terms of mass fraction (m_f) as previously researched in the literature [26,47,48]. In addition to those samples, Albipox 1000, Nanopox F700 by Evonik, which contain $m_f = 40\%$ rubber and silica respectively, and their equal mass mixtures are added to epoxy to manufacture these sets of composites. For this material group, the reinforcements are mixed in the epoxy resin by 5%, 10% and 15% (m_f). Studies with similar mass fractions can also be found in the literature [23,24]. So, nine more sample sets are prepared. In total, 22 sample sets are manufactured that would include the control ($m_f = 0\%$) sample. Weighing is done using a Mettler-Toledo Standard Level Balances ME Precision Balances with a capacity of 5200 g and precision between $0.001-0.01$ g. In each material manufacturing increment, 360 g of material is prepared.

2.1.1. Preparation of epoxy

The two components of the epoxy, the resin and the hardener are brought together and mixed until the colour homogeneity is achieved. The mixing is done slowly to avoid any air bubbles coming into existence at room temperature in ambient conditions. The mixture is then moulded and put into the vacuum chamber for 2 h. Afterwards, the mould is left in ambient conditions for 24 h for curing. Finally, the samples are put into the incubator at 60 °C for 15 h for the post-curing process.

2.1.2. Preparation of FS and HNT reinforced epoxy

Before starting the manufacturing process, the nanoparticles, namely FS and HNT, are put into an incubator and kept there for at least 8 h to ensure the minimisation of harboured humidity between the particles. The FS particles have an average diameter of 12 nm, and the HNT particles have diameters between 30–70 nm and lengths between 1–3 μm. The particles are blended into the resin component of the epoxy by using an electromagnetic mixer at 50 °C and 100 rpm for at least 2 h. An ultrasonic homogeniser is used to ensure a better distribution of particles and avoid agglomeration. During this process, the temperature of the mixture is controlled to prevent any chemical reactions that may be caused by excessive heating, which may strongly affect the mechanical properties of the epoxy resin. After, the mixture is degassed in the vacuum chamber for at least one hour. Following degassing, the hardener is mixed into the mixture slowly until colour homogenisation is achieved while trying to minimise the development of air bubbles. Then, the final moulded mixture is moulded and put into the vacuum chamber for two hours. Then, the same curing and post-curing processes are followed as done for the epoxy samples to achieve a consistent resin formation.

The mass composition of the composite described is presented in Table 1.

Table 2
Composition in mass of material depending on the reinforcements provided by Evonik (mass is measured in g.).

Mass fractions (m_f)	Matrix mass [g]		Reinforcement mass [g]		
	Epoxy resin	Hardener	Albipox 1000	Nanopox F700	Albipox 1000 and Nanopox 1000
0.05	217.29	97.71	45.00	45.00	45.00
0.1	177.43	92.57	90.00	90.00	90.00
0.15	137.57	87.43	135.00	135.00	135.00

Fig. 1. Some of the manufactured samples.

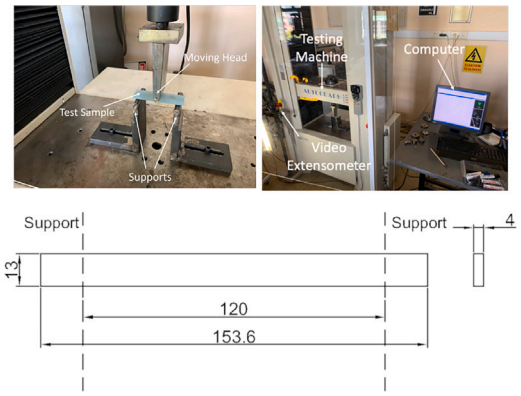

Fig. 2. Three-point bend test setup and sample (Dimensions in mm).

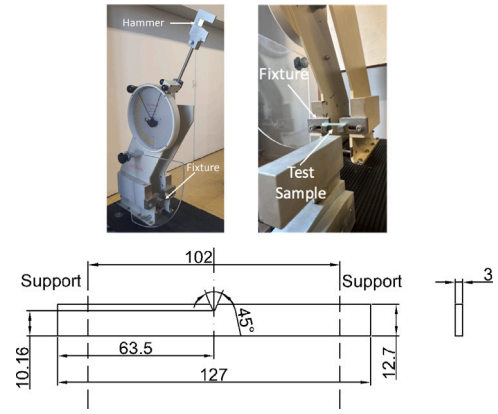

Fig. 3. Charpy impact test setup and sample (Dimensions in mm).

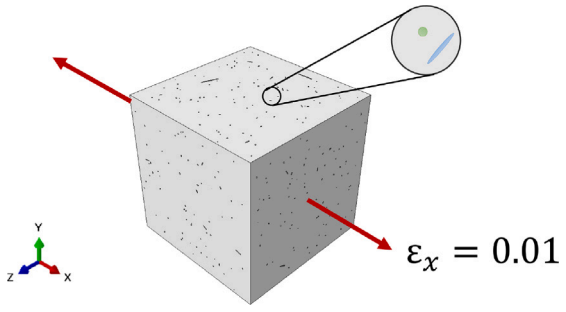

Fig. 4. A section view of a generated RVE with spherical and ellipsoidal inclusions.

2.1.3. Preparation of Albipox 1000 and Nanopox F700 mixed epoxy

It is simpler to manufacture this group of nanocomposite materials compared to the previously explained nanocomposite materials since the ultrasound homogeniser is not needed in this process. In the final state of the composite, it is expected that the silica particles in Nanopox F700 would have an average diameter of 20 nm and a maximum diameter of 50 nm. The rubber particles (Albipox 1000) have equivalent diameters between 0.5 and 1 μm. Albipox 1000 and/or Nanopox F700 are directly mixed mechanically into the resin component of the epoxy in the desired amounts. The mixing procedure is performed at 100 rpm and 50 °C for at least 4 h. This is with the same degassing, mixing of hardener, moulding, curing and post-curing processes followed to finalise the manufacturing of those samples.

The compositions of the manufactured composites are given in Table 2.

Some of the manufactured samples are shown in Fig. 1.

2.2. Scanning Electron Microscopy (SEM)

The internal structure of the composites strongly affects the mechanical properties of materials. Therefore, at least a basic understanding of the internal structure, which can be gained by SEM, is essential to be able to comment on the mechanical performance of materials. For this exact purpose, the internal structure of the manufactured composites is visualised using an SEM (FEI, Quanta Feg 250). In order to conduct visualisation of material morphology using SEM, the material surfaces are first coated with gold/palladium (Au–Pd) to ensure conductivity. The images are acquired at 20 kV potential difference.

2.3. Three-point bend tests

Considering polymers usually display complicated mechanical characteristics, which can be affected by numerous parameters, a simplistic yet accurate material model needs to be employed to predict their mechanical behaviour without creating computational difficulties. Strain rate is one of the dominant factors that form the models to be built on polymers. Therefore, in this study, the material behaviour is expected to be nonlinear. To understand the strain-rate-dependent mechanics of the manufactured composite materials, which are expected to have a nonlinear material behaviour, the material samples are put through three-point bend tests at three different strain rates, from a strain rate of 0.01 min^{-1} (sometimes referred to as quasi-static) up to 0.1 min^{-1} with equal increments based on the standard ASTM D7264 using the equipment Shimadzu AG-IS 50 kN which is displayed in Fig. 2 [49]. The strain rate range chosen is based on equipment capability, as well as consideration of previous research at similar strain rates, so the experimental data are comparable [30,50]. Thus, the effects of reinforcements on the nonlinear material behaviour are explored.

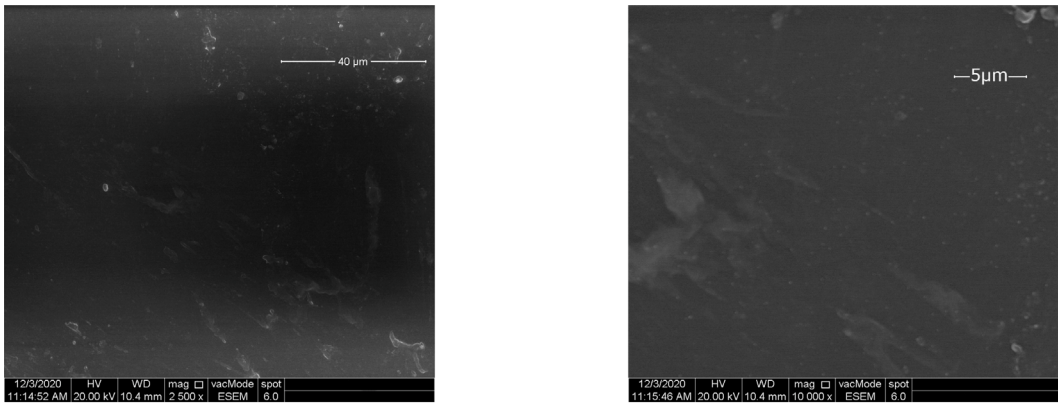

(a) Lower magnification. (b) Higher magnification.

Fig. 5. SEM images of an unreinforced epoxy sample showing homogeneous structure.

2.4. Charpy impact tests

Following the characterisation of strain-rate-dependent mechanical properties of the nanocomposites, Charpy impact tests are conducted to compare the fracture energies of specimens with different types and amounts of reinforcements. The effect of reinforcements on ductility is explored. Five samples from each of the 22 material groups are used to gather the necessary data from this test. The tests are performed with the setup shown in Fig. 3 as described by the standard ASTM-D6110 [51].

3. Material simulations

Theoretical modelling is also conducted using MFH and FE methods to investigate the mechanics of the prepared composites. The MFH is employed to predict the effective mechanical properties of the composites and their individual components, whereas FE method is used to predict the micromechanical behaviour as well as mechanical properties at the macro-level.

3.1. Mean-field homogenisation with Mori–Tanaka method

As one of the most common, computationally convenient and accurate methods to predict the mechanical behaviour of the composites, Mori–Tanaka MFH method is employed within the scope of this study. To predict the effective mechanical properties of the reinforcing particles and as a result, the manufactured composites, Mori–Tanaka homogenisation is performed [38]. The elastic moduli of the particles are iterated until the error between the experimental and numerical approaches is minimised. The epoxy matrix and all the inclusions are taken as linear elastic. The interfaces between the matrix and the particles are modelled using the rigid bonding approach for the sake of simplicity. Furthermore, except for HNT, which is taken into the calculations as ellipsoids, the rest of the inclusions are presumed as spheres. The dimensions for the specific inclusions can also be found in the corresponding datasheets as well as the literature [3,24]. Thus, a basis is built for a more detailed numerical investigation of the mechanics of the nanocomposites with the FE method.

3.2. Finite element analysis with representative volume elements

Inheriting the assumptions as well as the knowledge from the computationally faster method, Mori–Tanaka MFH, the FE models of the nanocomposites are built using RVEs with PBC under uniaxial tensile strain of 0.01 imposed on one surface. These RVEs are subjected to uniaxial tension so that the stresses in small-scale as well as the effective mechanical properties could be calculated. As the first step, a FE model of an RVE with randomly sized and positioned reinforcement particles is prepared. The random positions and orientations of the nanoparticles are arranged so that none of the particles intersects with each other, or the boundaries of the RVE [52–55]. This approach can be valid as long as the RVE parameter is chosen appropriately and the reinforcement volume fraction must not be too high, so a tight packing is not necessary and does not occur. Therefore, the RVE is constructed as a cube with a side length at least five times the largest particle dimension so that the RVE converges to the actual material behaviour [56,57]. Alongside the careful selection of safe RVE parameters, the analyses are conducted for each material set five times to ensure reliable and repeatable results. Fig. 4 shows a section view sample of an RVE generated for this study.

4. Results and discussions

4.1. Material testing and experimentation

4.1.1. Scanning Electron Microscopy (SEM)

The images acquired with higher and lower magnifications for each main reinforcement type are presented and interpreted starting from unreinforced epoxy, which is used as a reference for evaluating the mechanical properties of the nanocomposites. The SEM images of the surface of an unreinforced epoxy sample is given in Fig. 5. The images obtained with the lower magnification (Fig. 5(a)) and by magnifying the epoxy material by 10 000 times (Fig. 5(b)) reveal that formations such as voids and other features are not observed on the surface and the surface is macroscopically smooth. Thus, the hindering effects of cracks, voids or any similar sort of inhomogeneities are not expected in the results of the mechanical tests.

Based on the images shown in Fig. 6 acquired from the sample reinforced with FS, it can be seen that the surface is smooth and has a homogeneous structure and no undesirable material flaws, inhomogeneities, or cavities are visible. The image with lower magnification shows a larger area, however cannot display any reinforcements. Meanwhile in Fig. 6(b), the FS particles are visible as white dots, which appear to have an average size of just above 10 nm. Clustering is also not observed, and the reinforcing particles display a relatively evenly spaced dispersion. These findings suggest that the variations in the mechanical performance of the composite will be strongly correlated to the presence of the reinforcing particles.

The SEM images of an HNT reinforced epoxy composite are presented in Fig. 7. Fig. 7(a) shows a smooth surface and a homogeneous structure. The HNT particles are visible as faint lines and dots only in Fig. 7(b). Compared to the sample with FS, the composite containing HNT displays a lesser homogeneous structure. On the positive side, neither agglomeration nor major cavities or any sort of defects are

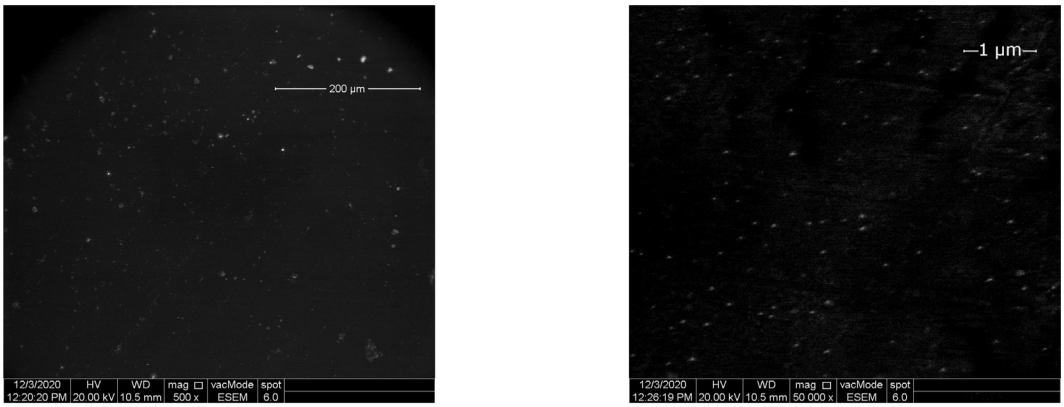

(a) Lower magnification. (b) Higher magnification.

Fig. 6. SEM images of an epoxy sample reinforced with FS (seen as dots with diameter of approximately 10 – 15 nm).

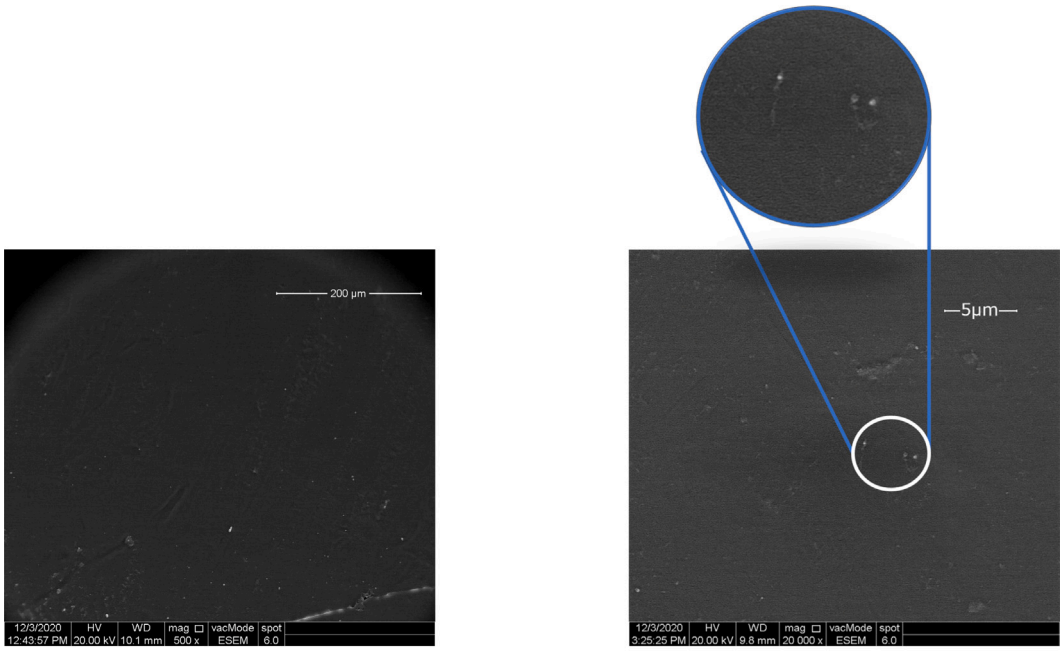

(a) Lower magnification. (b) Higher magnification.

Fig. 7. SEM images of an epoxy sample reinforced with HNT (visible as dots and lines with diameter of approximately 30 – 70 nm and length of approximately 1 – 3 µm.

visible, which strengthens the argument that the particles control the change of mechanics of the composite compared to unreinforced epoxy.

In Fig. 8, the SEM images of epoxy with rubber addition are displayed. Fig. 8(a) displays a relatively smooth surface over the larger scale. The formation of rubber is visible in Fig. 8(b) as grey sectors with a size below 1 µm and the surface have superficial irregularities, whereas again, no major material defects such as clustering, cavities or cracks. Thus, one can expect no significant hindrance to mechanical properties due to material flaws caused by the manufacturing processes.

The last SEM images are gathered from the epoxy-based composite reinforced with silica and is given in Fig. 9. While Fig. 9(a) displays a larger portion of the surface and clarifies that the structure is homogeneous and the surface is smooth, the silica particles are seen as grey and white dots of the size 20 nm in Fig. 9(b). The surface appears to be relatively smooth and homogeneous without any notable material defects. Besides, it is clearly seen that the silica nanoparticle reinforcements have almost a uniform distribution. This substantiates the idea that the manufacturing of the composite is overall successful with respect to uniform mixing. The mechanical performance is predicted not to be impacted by non-uniform distributions of the reinforcement in the matrix.

Finally, the SEM results suggest that the composites are overall manufactured without significant irregularities visible in their morphologies. Thus, comparing their mechanical behaviours based on the reinforcements becomes a valid approach.

4.1.2. Three-point bend tests

The results of the three-point bend tests aim to characterise the rate-dependent mechanics of the manufactured epoxy-based composites and are presented in this section. Figs. 10–15 exhibit the stress–strain plots of the unreinforced epoxy and the composites for the three strain rates, (0.01 min^{-1}, 0.05 min^{-1} and 0.1 min^{-1}). The curves of unreinforced epoxy given in Fig. 10(a) suggest that the unreinforced epoxy acts stiffer and becomes more brittle, which leads to failure at a lower deformation particularly at higher strain rates. Furthermore, the strength is also found to be greater at higher deformation rates.

The data in Fig. 10 suggests that both tensile strength and Young's modulus rise with increasing mass fraction of FS reinforcement, as well as with increasing strain rate, particularly at the highest mass fraction.

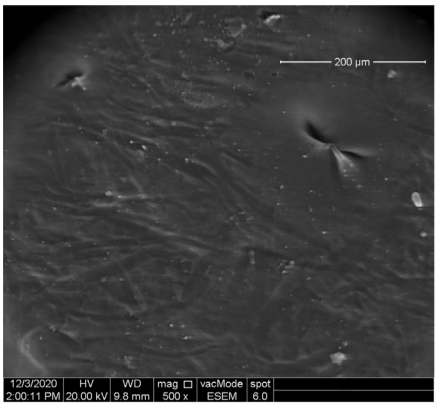

(a) Lower magnification.

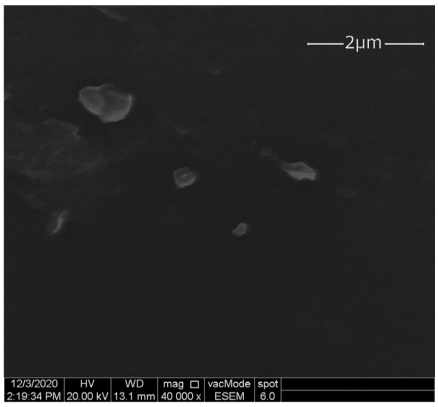

(b) Higher magnification.

Fig. 8. EM images of an epoxy sample reinforced with rubber (seen as regions with lighter colour with diameter of approximately $0.5 - 1$ µm).

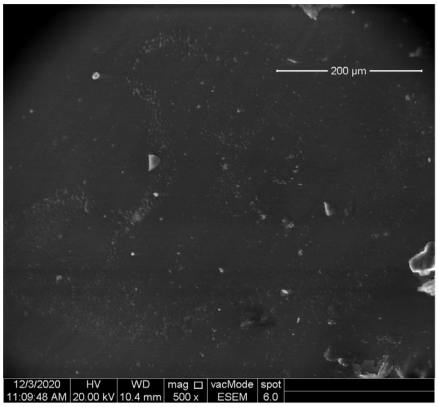

(a) Lower magnification.

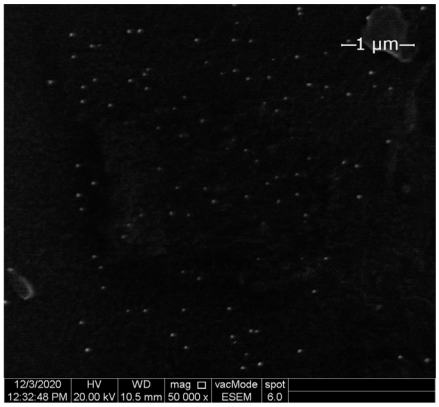

(b) Higher magnification.

Fig. 9. SEM images of an epoxy sample reinforced with silica (visible as dots diameter of approximately $20 - 30$ nm).

It is also important to note that the elongation at break also increases with more FS particles present. The material is observed to behave in a more brittle way with an increasing strain rate.

The stress–strain curves of epoxy nanocomposites reinforced with HNT are presented in Fig. 11. The tensile strength and rigidity increase with the mass fraction of HNT. A similar trend is also noticed at higher rate deformations. The change in these parameters is more marked than for nanocomposites reinforced with FS. On the other hand, the elongation at break values drop with increasing strain rates. Meanwhile, the addition of HNT influences the elongation at break in a more complicated way. The elongation at break peaks when the composite includes $m_f = 0.5\%$ HNT and then drops slightly when more HNT is added. The elongation at break hits the minimum under the greatest strain rate and in the absence of HNT. Therefore, it appears as if the behaviour is controlled by HNT at lower mass fractions whereas with increasing amount of reinforcements, FS takes over dominance of the behaviour regarding elongation at break.

Aiming to further investigate the synergistic effects of FS and HNT inclusions together, Fig. 12 is presented, which shows the stress–strain graphs of the epoxy-based nanocomposites that are reinforced with FS and HNT inclusions in equal masses and put through the experimental procedure with different strain rates. Based on the data, the composite is found to be stronger and stiffer with the growing amount of reinforcement along with rising strain rates. The findings reveal that the elongation at break falls with the pace of strain speeding up. These magnitudes of growth in both strength and stiffness are found mostly in between the results of the composite reinforced with FS and the one with HNT. While all these describe monotonic trends, the mass fraction of reinforcement-elongation at break has a more complex relation. Elongation at break reaches a local maxima at $m_f = 0.5\%$ mass fraction of the reinforcements, and then it drops at $m_f = 1.5\%$ reinforcement constant (RC) where it rises again. This behaviour can be understood by referring to the previously explained composites, which are reinforced with either FS or HNT. The peak at $m_f = 0.5\%$ is a characteristic of the composite reinforced with HNT, while the monotonically increasing trend is the composite type reinforced with FS. Therefore, one can claim that the behaviour is controlled by HNT at lower mass fractions whereas with increasing amount of reinforcements, FS takes over the domination of the behaviour regarding elongation at break.

The stress–strain results of three-point bend tests conducted on samples made of epoxy reinforced with rubber (Albipox 1000) particles are presented in Fig. 13. This material group differs significantly from others due to the relative stiffness of the reinforcing phase. In all other material groups, the reinforcing material is stiffer and stronger than the matrix material. The first major difference is that the strength alongside stiffness drop with increasing rubber particle content in the composite. Secondly, both strength and stiffness build up with increasing strain rates. Consequently, they reach the maximum values with unreinforced epoxy under 0.05 min^{-1}. Although the material becomes weaker and more compliant with more rubber particles, the ductility is significantly increased. As a result, elongation at break peaks at the most rubber content under 0.01 min^{-1} loading. The elongation at break values are above 0.10, which is greater compared to the composites reinforced with FS, which also display increasing ductility. It must be noted that the amounts of reinforcements used in this group of composites are significantly more than the mass of reinforcements used in composites with FS.

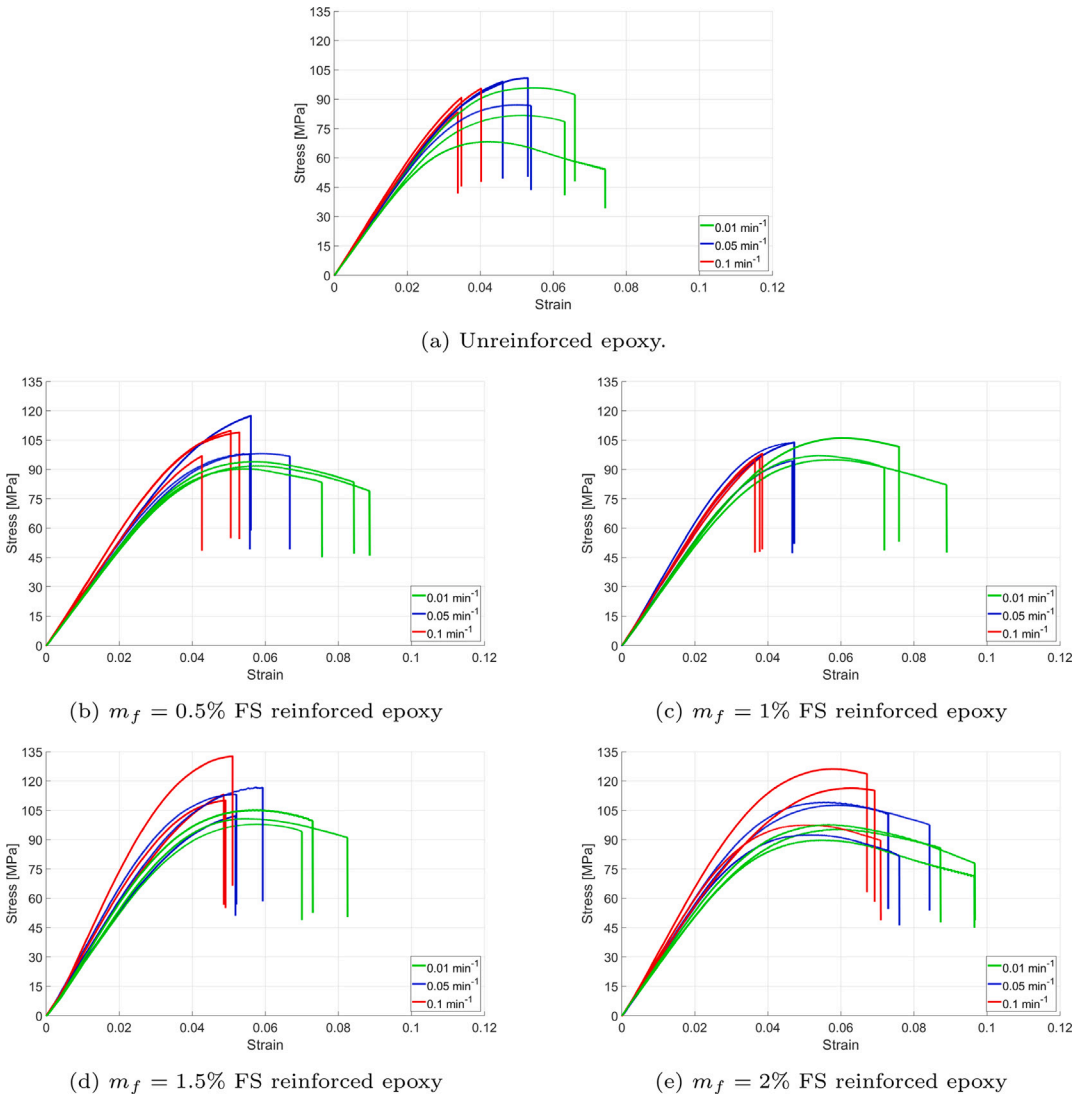

(a) Unreinforced epoxy.

(b) $m_f = 0.5\%$ FS reinforced epoxy

(c) $m_f = 1\%$ FS reinforced epoxy

(d) $m_f = 1.5\%$ FS reinforced epoxy

(e) $m_f = 2\%$ FS reinforced epoxy

Fig. 10. Stress–strain curves of FS reinforced epoxy.

The stress–strain data of the next group of epoxy-based composites with a different type of nano-silica is given in Fig. 14. The general tendency is that the material stiffens and the ultimate flexural stress increases with rising deformation speeds and reinforcement presence which is similar to the behaviour observed in material groups reinforced with FS. The only difference to be noted is a slight drop in stiffness at $m_f = 5\%$ silica reinforcement. Also, the fall of the elongation at break values with increasing strain rates exhibit similar behaviour to the composites with FS. However, moving onto the elongation at break, it becomes clear that a similar trend to the FS reinforced epoxy is no longer evident. The values of elongation at break hits its minimum when the reinforcement is at $m_f = 5\%$ and then climbs up at $m_f = 10\%$ RC and then falls again at $m_f = 15\%$ silica content.

The final set of materials, epoxy reinforced with rubber and silica (Albipox 1000 and Nanopox F700) is shown in Fig. 15. These are the stress–strain curves obtained from the three-point bend experiments. As the rest of the material groups, this one also displays the same behaviour with increasing strain rate. Specifically, the material's strength and stiffness values rise, whereas the elongation at break falls with faster deformations. However, the addition of reinforcements influences material behaviour in a more complicated manner. The stiffness declines and hits its minimum at $m_f = 5\%$ reinforcement and under $0.01\ \text{min}^{-1}$ loading. Adding more reinforcements to the composite, the stiffness starts to ascend slightly, though, the flexural strength shows an entirely different characteristic. It peaks under $0.1\ \text{min}^{-1}$ and decays with lowering strain rates. However, the RC does not significantly affect the materials' strength. Meanwhile, elongation at break has its peak where the loading is $0.01\ \text{min}^{-1}$, and the reinforcement mass fraction is $m_f = 10\%$. This complex behaviour of the three mechanical properties can be explained by the synergistic effect of the two reinforcing particles having opposite characteristics and effects. For instance, the stiffness drops at lower reinforcement masses with increasing particle content. This is parallel to what is observed in composites with Albipox 1000. Later, with more particles in the material, Young's modulus starts to recover after reaching the trough, suggesting that the silica influence overcomes rubber dominance. A similar explanation can be given for the trends in elongation at break. The elongation at break values of composite mixed with Nanopox F700 reach a maximum at $m_f = 10\%$ RC in terms of mass which is followed by a fall with increasing reinforcing particles. Whilst the composite that consists of Albipox 1000 exhibit a monotonically increasing trend against the rubber content. Hence, coming together, these two particles lead to the characteristic described reaching its maximum at the RC of $m_f = 10\%$.

The results presented in this section so far are found to be in good agreement to the previous research. The results in the literature also suggest that the material behaves stiffer and the elongation at break values drop with increasing strain rates [30,50]. Also, the changes of

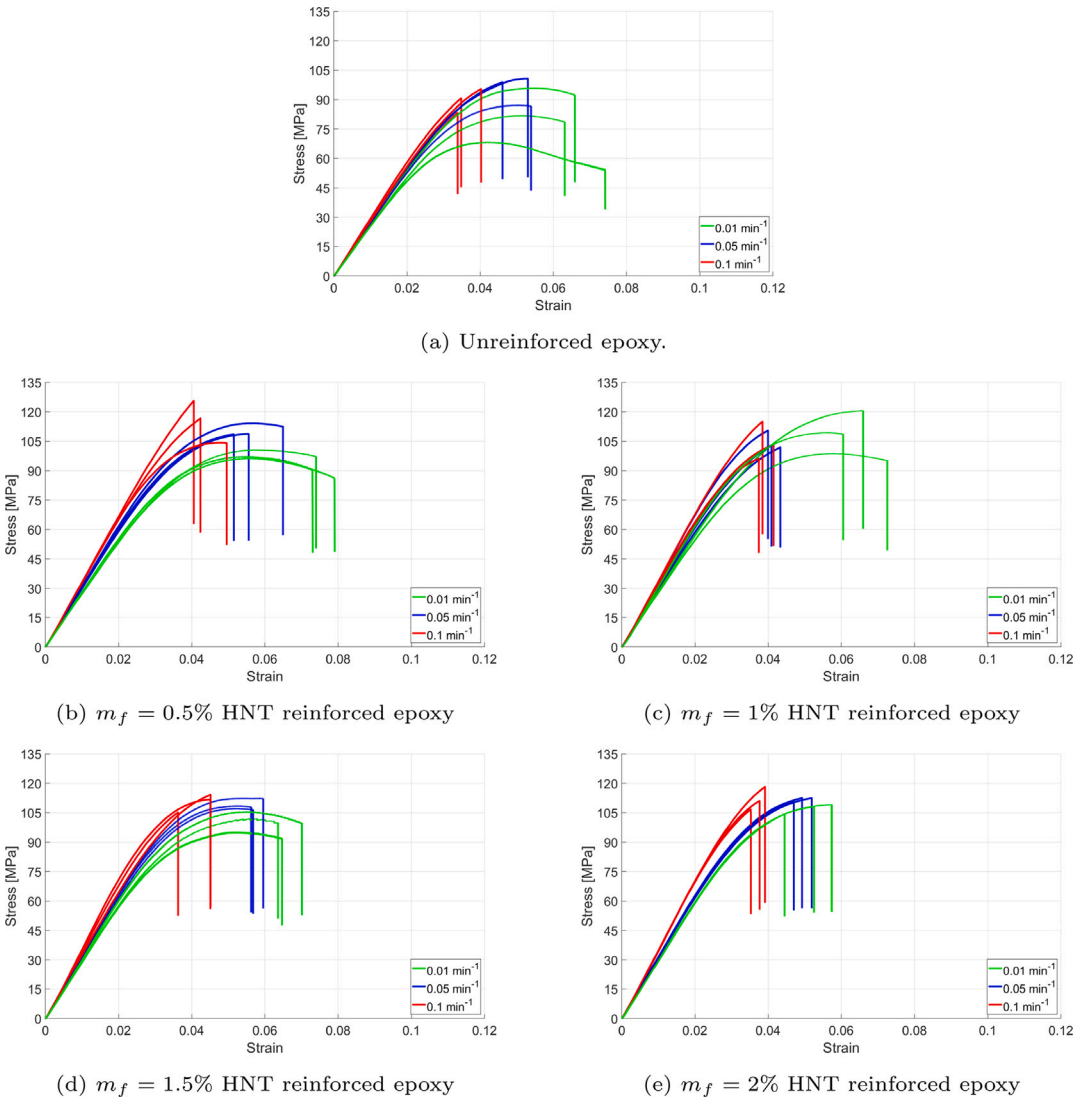

(a) Unreinforced epoxy.

(b) $m_f = 0.5\%$ HNT reinforced epoxy

(c) $m_f = 1\%$ HNT reinforced epoxy

(d) $m_f = 1.5\%$ HNT reinforced epoxy

(e) $m_f = 2\%$ HNT reinforced epoxy

Fig. 11. Selected stress–strain curves of HNT reinforced epoxy.

the stiffnesses and the ductilities of the composites with the addition of silica and HNT can be found [11,24,47].

Overall, the findings of the three-point bend tests with different strain rates are found compatible with the literature. With more rigid particles like silica and HNT, it is expected that the shear band yielding and plastic void growth due to debonding of the particles are the primary toughening mechanisms [58–60]. In addition, stiffer and stronger particles contribute to the effective stiffness of the material but due to the debonding, the contribution of the particles to the strength of the material remain limited. Whereas the presence of the rubber particles lead to the activation of a different toughening mechanism due to better interface bonding properties with the epoxy matrix and lower stiffness. Cavitation initiates within the rubber particle and the interface debonding is usually not observed [24,61]. Thus, plastic void growth initiating in the particles is expected to be the dominant toughening mechanism alongside the localised plastic shear bands. Apart from these, the effects of the strain rate also shows good agreement to the literature. A decline of ductility with rising strain rates is observed similar to the research available in the literature [62].

Finally, the fracture surfaces of one sample from each material group with different reinforcement types displaying opposite characteristics in terms of ductility and stiffness are shown in Fig. 16. $m_f = 1\%$ HNT-reinforced (Fig. 16(a)) and $m_f = 10\%$ rubber-added (Albipox 1000) Fig. 16(b) epoxy samples are selected since HNT increases the stiffness and reduces the ductility and rubber has the opposite effect. The images show that the fracture surface of the brittle material (HNT-reinforced epoxy) is brighter and more reflective and the cross-section is less deformed/warped than the ductile material which is a consequence of the high stiffness of the HNT particles that contribute to the effective stiffness of the composite.

4.1.3. Charpy impact tests

After investigating the strain rate-dependent mechanics of the epoxy and epoxy-based composites, the impact behaviour of those materials is also investigated, and the results are presented in this section. The measured impact energy for FS and HNT reinforced epoxy is shown in Fig. 17. The data in Fig. 17 suggests that the addition of FS, even in small amounts, increases the impact energy dramatically. It is observed that adding more FS into epoxy resin makes the impact energy rise almost in a linear manner. On the other hand, HNT-doped epoxy shows a distinctively different characteristic. It can be claimed that the presence of HNT slightly increases the impact energy, but the trend is not linear between the mass of HNT reinforcement and the resulting impact energy. The relation looks rather more like a saturation behaviour. The presence of $m_f = 0.5\%$ HNT appears to be enough to bring the impact energy to its upper boundary. The final curve in Fig. 17 displays the impact energy measured from the epoxy samples reinforced with FS and HNT, which demonstrates the synergistic effect caused by the

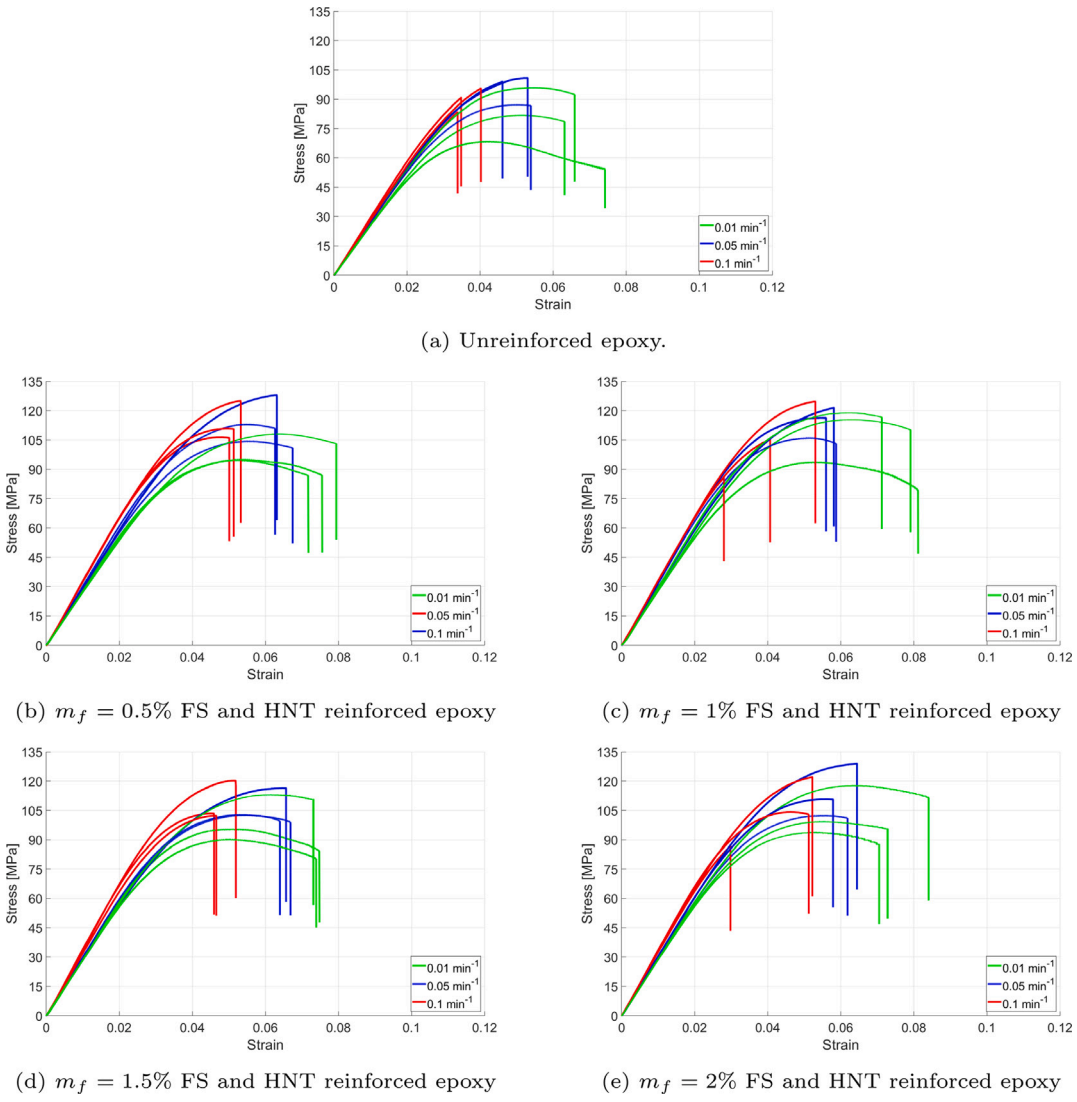

(a) Unreinforced epoxy.

(b) $m_f = 0.5\%$ FS and HNT reinforced epoxy

(c) $m_f = 1\%$ FS and HNT reinforced epoxy

(d) $m_f = 1.5\%$ FS and HNT reinforced epoxy

(e) $m_f = 2\%$ FS and HNT reinforced epoxy

Fig. 12. Selected stress–strain curves of FS and HNT reinforced epoxy.

presence of two different particles in the resin. The results show that adding these two particles into epoxy has a more significant synergistic influence on the materials' impact energy. The impact energy rises by almost 50% with the presence of a $m_f = 0.5\%$ mass fraction of those particles. The impact energy keeps increasing if more particles are involved in the composite. However, the growth rate of the impact energy drops with increasing mass fractions of particles. Thus, the effect of both particles becomes visible, the almost-linear increasing trend of FS and the saturation behaviour in the presence of HNT.

Similarly, Fig. 18 shows the impact test results of the epoxy reinforced with silica and rubber. In these material groups, the change of impact energy depending on the inclusion mass fraction appears similar when compared to the previous composites. The impact energy increases with increasing inclusion content. The rise, however, occurs with a declining rate. The results suggest silica reinforcement is the most preferable reinforcement type for improving energy absorption under impact. Rubber also provides some improvement in terms of impact energy which is slightly less than silica. Using both rubber and silica particles in the composite leads to an intermediate behaviour between only silica-reinforced and only rubber-added composites with respect to impact energies.

Generally, the findings of the Charpy impact tests are in good agreement with results presented in the literature. Similar comments as in Section 4.1.2 can be made regarding the toughening mechanisms of the composite materials depending on the type of the particles added as reinforcements.

Fig. 19 exhibits the cross-sections of the fracture surfaces of the samples reinforced with $m_f = 1\%$ HNT and $m_f = 10\%$ rubber (Albipox 1000). These material groups are selected for the same reasons as explained in Section 4.1.2. As observed for the three-point bend cases, the fracture surface of the more ductile material, which is epoxy with rubber (Albipox 1000) particles, is deformed more and is duller compared to the fracture surface of the HNT-reinforced epoxy composite sample.

4.2. Material simulations

As discussed in Section 3, MFH (Mori–Tanaka) studies are first conducted on each composite group to determine the elastic properties of the reinforcements. Finally, the approximated values of the elastic modulus for the particles are determined. The Young's moduli for FS, HNT, rubber (Albipox 1000) and silica (Nanopox F700) are found to be 70 GPa, 1000 GPa, 200 MPa and 10 GPa respectively. These values are employed for all the numerical analyses conducted for this study.

Determining the elastic properties of the particles, the homogenised mechanical properties of the composites are calculated for each material group under each strain rate using both Mori–Tanaka and FE

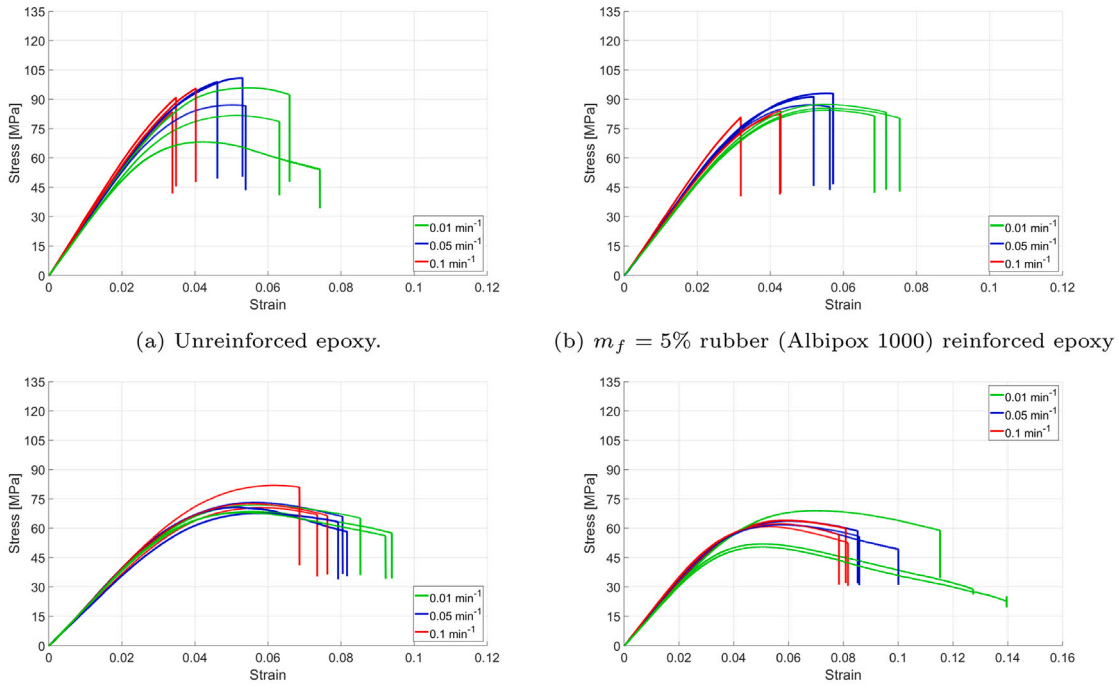

(a) Unreinforced epoxy. (b) $m_f = 5\%$ rubber (Albipox 1000) reinforced epoxy

(c) $m_f = 10\%$ rubber (Albipox 1000) reinforced epoxy (d) $m_f = 15\%$ rubber (Albipox 1000) reinforced epoxy

Fig. 13. Selected stress–strain curves of rubber (Albipox 1000) reinforced epoxy.

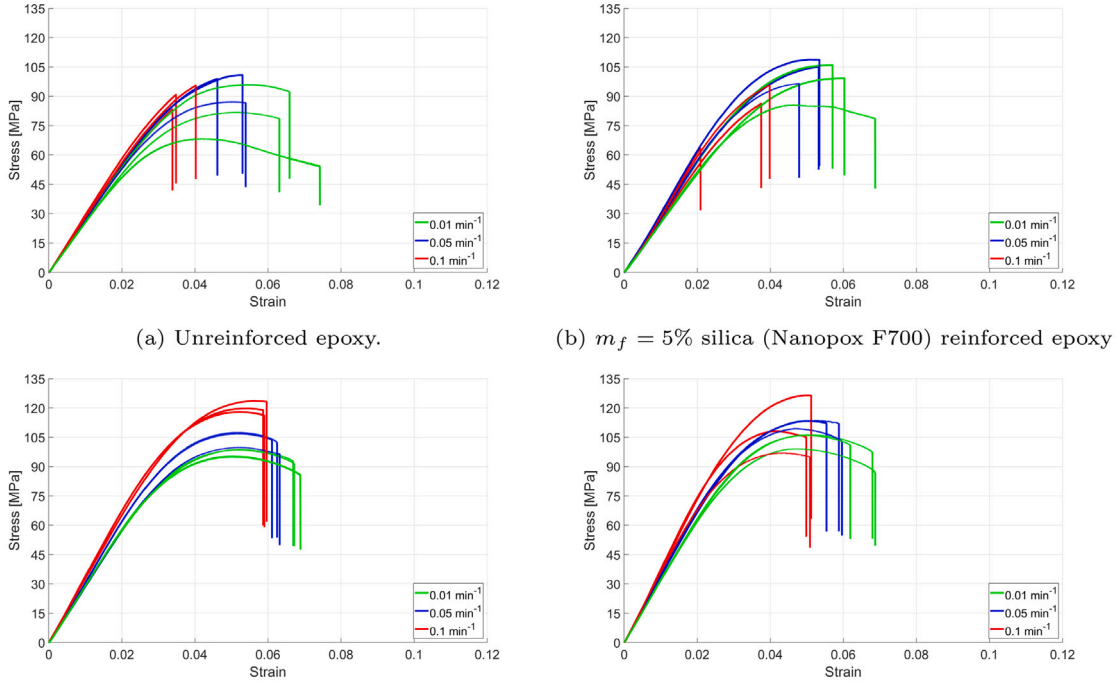

(a) Unreinforced epoxy. (b) $m_f = 5\%$ silica (Nanopox F700) reinforced epoxy

(c) $m_f = 10\%$ silica (Nanopox F700) reinforced epoxy (d) $m_f = 15\%$ silica (Nanopox F700) reinforced epoxy

Fig. 14. Selected stress–strain curves of silica (Nanopox F700) reinforced epoxy.

methods. Figs. 21–29 present the theoretically calculated effective moduli of elasticity and compare them to the experimentally determined elastic moduli of the composites. A view of the stress analysis results of an RVE reinforced with FS is presented in Fig. 20. Moreover, the data in Fig. 21 suggests that for FS reinforced epoxy nanocomposites, and both numerical methods yield results that are in good agreement with the experimental results showing deviation of approximately 7%. However, FE delivers a more accurate representation compared to the MFH. FE models have less simplifying assumptions compared to the MFH and FE conducts a more detailed stress analysis [45,46]. Therefore, this would be an expected outcome of the analyses conducted. It is noteworthy that FE is computationally way more expensive than MFH, and the error increases with increasing strain rates. This is explained by the nonlinear behaviour of the composite interphase regions, which affect the behaviour of the composite more with increasing strain rates, whereas the numerical models do not consider the nonlinear interphase

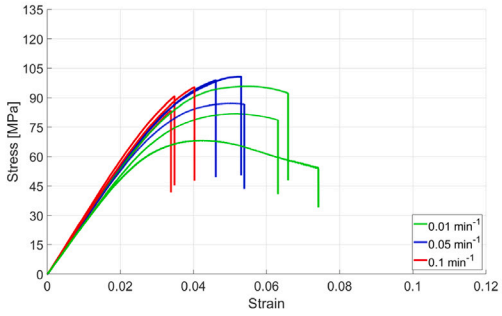

(a) Unreinforced epoxy.

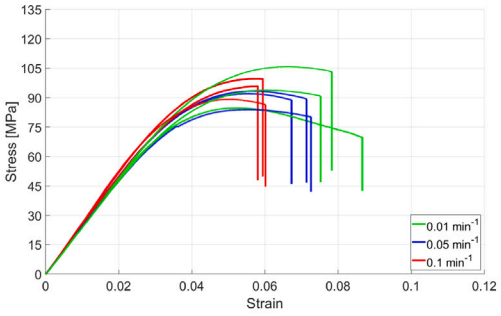

(b) m_f = 5% rubber and silica (Albipox 1000 and Nanopox F700) reinforced epoxy

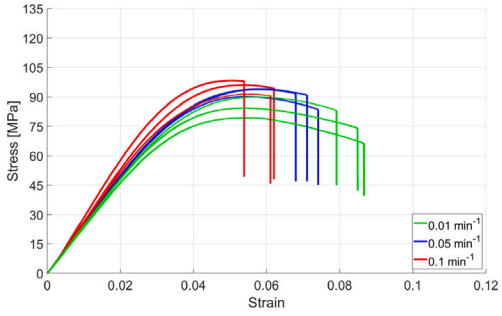

(c) m_f = 10% rubber and silica (Albipox 1000 and Nanopox F700) reinforced epoxy

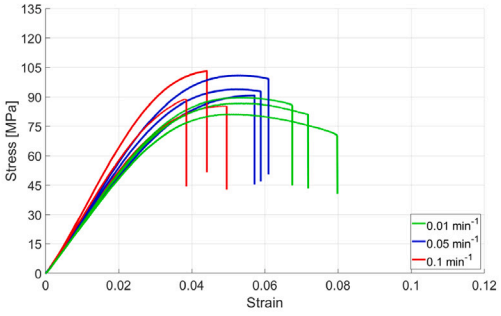

(d) m_f = 15% rubber and silica (Albipox 1000 and Nanopox F700) reinforced epoxy

Fig. 15. Stress–strain curves of rubber and silica (Albipox 1000 and Nanopox F700) reinforced epoxy.

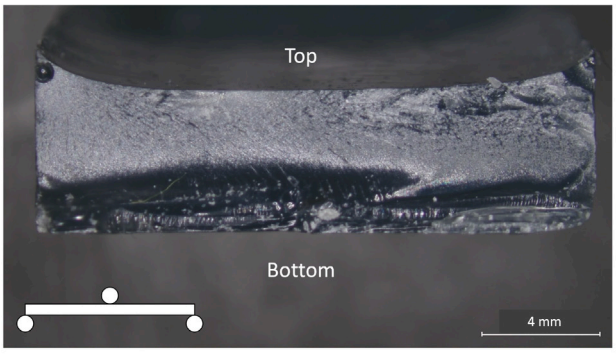

(a) Fracture surface of the three-point bend sample reinforced with HNT.

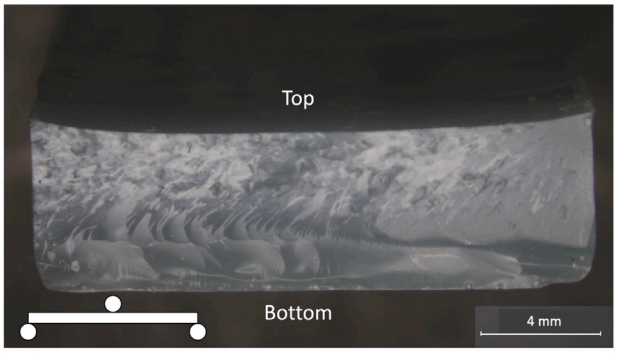

(b) Fracture surface of the three-point bend sample reinforced with rubber (Albipox 1000).

Fig. 16. Fracture surfaces of the selected three-point bend samples.

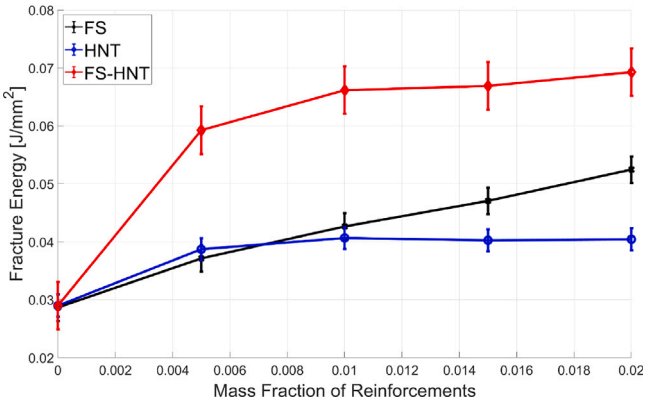

Fig. 17. Fracture energy from Charpy testing of composites reinforced with FS and/or HNT for increasing mass fraction.

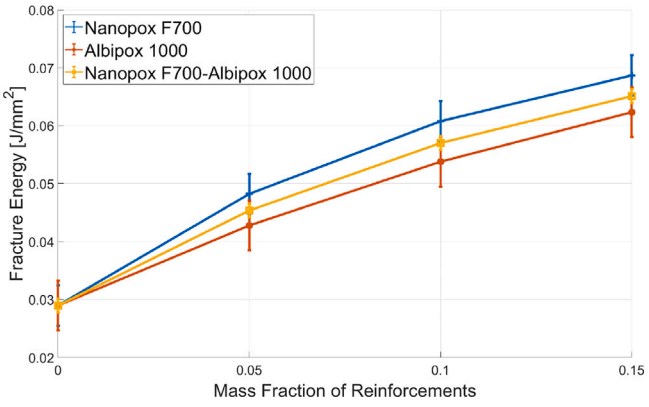

Fig. 18. Fracture energy from Charpy tests of composites reinforced with silica and/or rubber (Nanopox F700 and Albipox 1000) for increasing mass fraction.

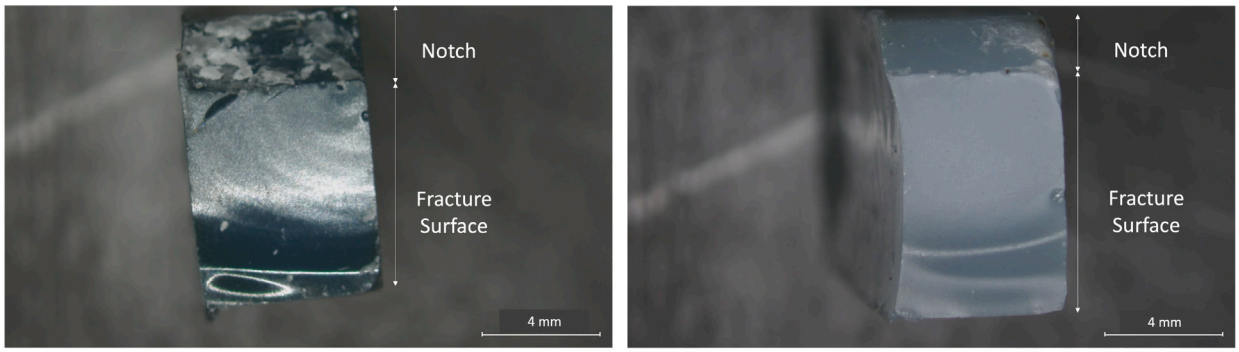

(a) Cross-section and the fracture surface of the Charpy sample reinforced with HNT.

(b) Cross-section and the fracture surface of the Charpy sample reinforced with rubber (Albipox 1000).

Fig. 19. Cross-sections and the fracture surfaces of the selected Charpy samples.

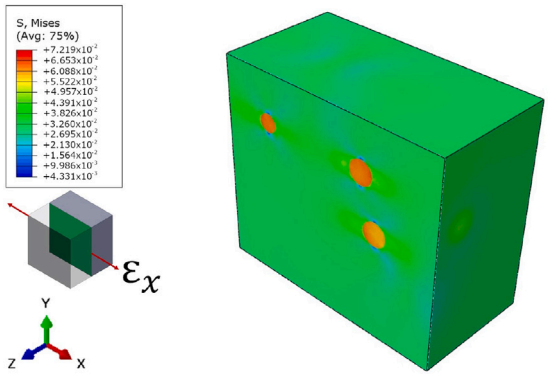

Fig. 20. A section view of an RVE with spherical FS inclusions with an average diameter of 12 nm taken between 10 – 15 nm (Stress unit: GPa).

regions [15]. Based on the FE analyses, the stress reaches its maximum in the inclusions which means the inclusions play a role in bearing the load. More importantly, significant triaxial stress concentrations, which lead to local plastic deformations that initiate in the polar region of the spherical inclusions, occur in the matrix. It is also observed that the magnitude of stress concentrations mainly depends on the size of the inclusion as well as the sizes of the nearest inclusions and the distances to the nearest inclusions. The stress concentrations around the inclusions in the matrix interact with each other depending on the distances between the particles of interest. The closer the particles, the stronger is the interaction. This emphasises the importance of a uniform distribution of the positions of particles.

Fig. 22 presents a section plot of the stress analysis performed with FE methodology and Fig. 23 presents the results of HNT reinforced epoxy composites and compares them to the experimental results. The maximum error between the numerical and the experimental results is around 9%. Here, the results are in good agreement. Especially the results of MFH and FE match quite well. However, the magnitude of error is more significant compared to the composites with FS and the deviation of error between the numerical and experimental results does not follow a perfect trend. The reason for this is the deviations in the experimental results. The results of both numerical methods follow a similar trend as mentioned earlier. However, the experimental results display less of this trend and therefore, the error grows. The FE results show that the maximum stresses are in the inclusions and these stresses are greater when compared to the ones observed in FS inclusions. This is due to the greater elastic modulus of HNT over FS. Moreover, the stress concentrations in the matrix occur around the tips of the ellipsoidal inclusions. Due to the geometry and greater difference in stiffness, the concentrations display larger values of stress. Also, due to the sharper geometry of the tip of the HNT inclusions, the stress triaxiality is stronger, which explains the more brittle behaviour. Unlike the case with FS, there are some additional parameters that are decisively influential on the stress concentration. The size of the HNT inclusions is one of those parameters. Since these are considered ellipsoidal particles, the size affects the radius of curvature at the tip. The radius of curvature for the aspect ratios that HNTs have is already quite small and therefore has a limited effect. The orientation of the HNT particles relative to the uniaxial loading direction is also one of those parameters. If the HNT inclusion lies perpendicular to the loading direction, the stress concentration tends to be smaller, and if the HNT

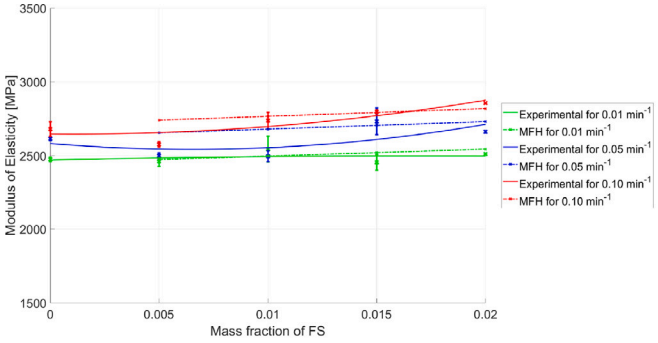

(a) Experimental versus MFH.

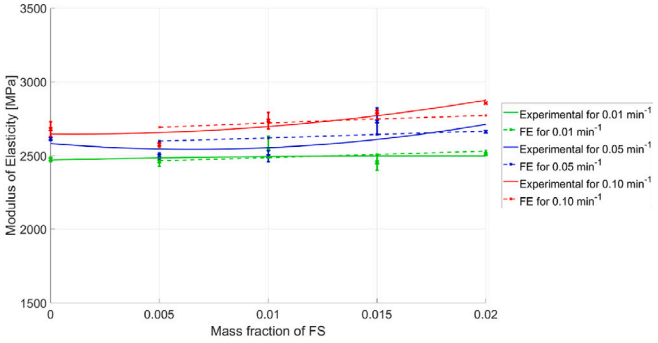

(b) Experimental versus FE

Fig. 21. Comparison of experimental results for modulus of elasticity with the numerical simulations of FS reinforced epoxy.

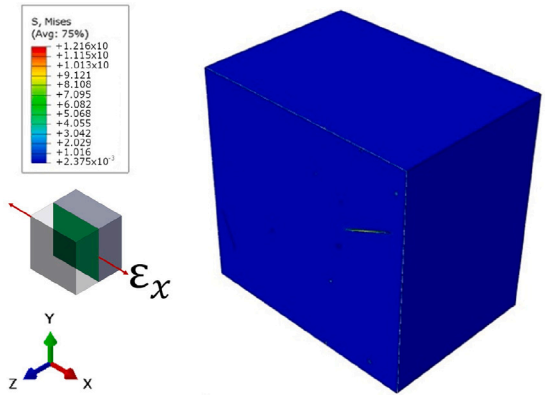

Fig. 22. A section view of an RVE with ellipsoidal HNT inclusions with diameters from 30 nm to 70 nm and lengths from 1 μm to 3 μm (Stress unit: GPa).

inclusion lies parallel to the loading direction, the stress concentration gets its peak value possible for that size of HNT inclusion. It is also worth mentioning that if the HNT particle orientation is parallel to the uniaxial loading direction, its contribution to the load-bearing capacity of the material in that direction is maximum and thus, the maximum stress possible is observed. However, if the orientation is perpendicular to the loading direction, the load that the HNT particle carries will be less and therefore, the stress in the HNT particle is less than what it would be if the orientation was parallel to the load.

Furthermore, Fig. 24 displays experimentally determined and numerically calculated Young's moduli results for the FS and HNT reinforcement combination. The results are found to be in good agreement with the maximum error of slightly less than 8%. Similar to the previous results, FE yields less error compared to MFH, which means it is capable of capturing the synergistic effect of multiple reinforcing phases better than MFH. The magnitude of error rises with growing strain rates for the same reason as with FS reinforced epoxy, the nonlinear interphase region. The nonlinearity of the interphase region becomes more significant with increasing strain rates, and therefore it influences the overall behaviour of the composite. The FE stress analyses indicate that the presence of both particles in the resin shows an intermediate behaviour compared to the two other individual cases. The interaction of stress concentrations at the tips of HNT is mostly reduced by the presence of FS particles. Thus, the stress concentrations interact in a more mild manner which reduces the brittle behaviour. The presence of HNT increases the effective stiffness of the composite.

Looking at another material group, Fig. 26 contains the results of experimental and numerical procedures. The maximum error between the numerical and experimental results is just below 19%. Unlike others, this material group displays a different behaviour in terms of error variation between the numerical and experimental. Overall, the error increases with the rising rubber inclusion content. The main reason is that the rubber reinforcement is more compliant than the matrix. Therefore, the stress peaks in the regions adjacent to the inclusions around the equatorial region of the inclusions in the matrix cause local plastic deformations [61]. Thus, the inclusions do not really contribute to the load-carrying capacity of the composite and weaken it instead. The rubber particles act like voids to this extent. Thus, the local plastic deformations make ground and visibly affect the effective mechanics of the composite. These findings are supported by the FE stress analyses. It must be emphasised that Albipox 1000 contains a resin which is compatible with most varieties of epoxies. Although it is compatible with the epoxy resin used in this study, it does not have to possess the exact same mechanical characteristics. This resin can be one of the reasons of the increasing error with increasing Albipox 1000 content. Fig. 25 shows a representative view of stress analysis of an RVE containing rubber particles.

The effective moduli of elasticity of the composites reinforced with silica (Nanopox F700) are given in Fig. 28. Overall the results agree and show similar trends with a maximum error of approximately 13%. Similar to the other cases MFH and FE show a better match against the experimental results. The relatively high error can be explained by the resin that Nanopox F700 has. This can also be the reason for the lower modulus of elasticity predicted for silica particles. Compared to FS, silica particles of Nanopox F700 are more compliant since the numerical models only include the stiffness of inclusions as a variable and do not consider any other resin that could be mixed into the composite. Other than these variances, the same comments made on FS reinforced epoxy can be made for this material group as well. An RVE is given in Fig. 27 to show a representative stress distribution for silica-reinforced epoxy nanocomposites.

Finally, to comment on the synergistic effect of rubber and silica particles, Fig. 29 is presented. The maximum error between the numerical and experimental results is approximately 9%. The error increases with increasing strain rates and decreases with increasing RC. The increasing error with increasing strain rate can be explained by the interphase nonlinearity, which is not included in the numerical models. Furthermore, the decreasing error with increasing RC is expected to be caused by the synergistic effect of the existence of two different particles with opposite mechanical characteristics. The stress analyses show

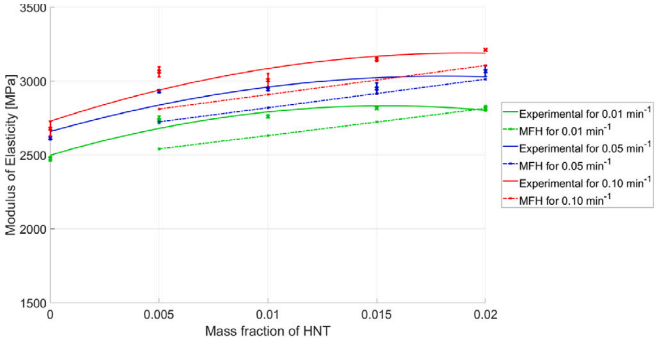

(a) Experimental versus MFH.

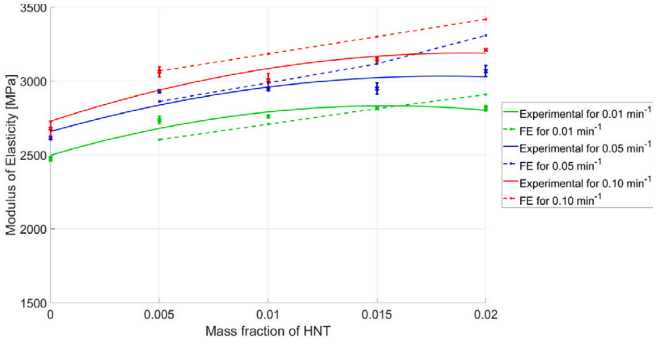

(b) Experimental versus FE

Fig. 23. Comparison of experimental results for modulus of elasticity with the numerical simulations of HNT reinforced epoxy.

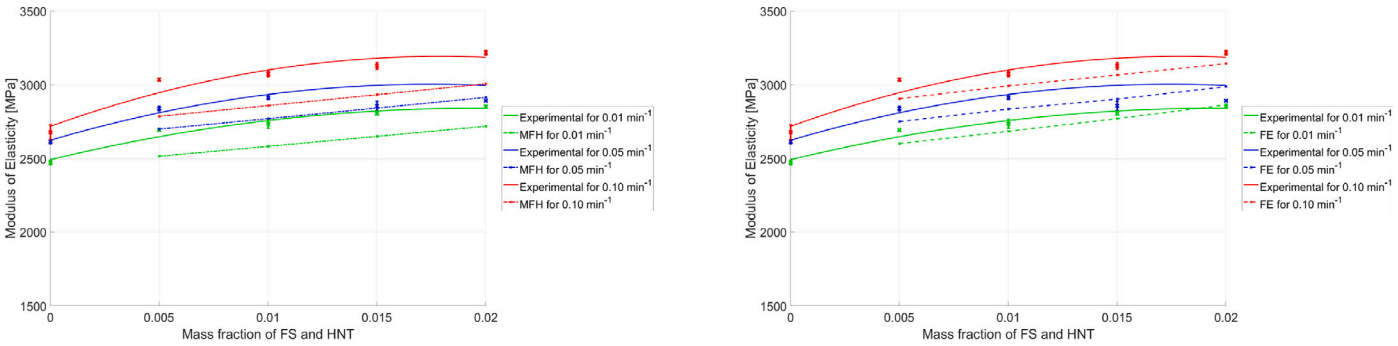

(a) Experimental versus MFH. (b) Experimental versus FE

Fig. 24. Comparison of experimental results for modulus of elasticity with the numerical simulations of FS and HNT reinforced epoxy.

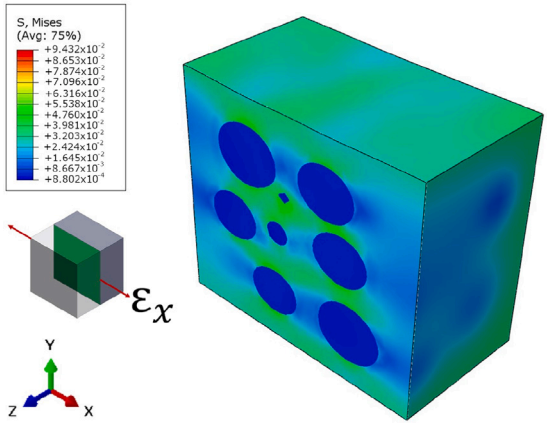

Fig. 25. A section view of an RVE with spherical rubber inclusions with diameters between 500 nm and 1 μm (Stress unit: GPa).

that the silica particles have higher stresses and the rubber particles have lower stresses. Similar to the other cases, the stress concentrations occur at the equatorial regions of the rubber inclusions and interact based on the size and distance between the particles. For the silica inclusions, the stress concentrations appear in the polar regions, and the stress distribution is affected the same way by the interactions of stress concentrations.

5. Conclusions

This study focusses on the manufacturing and strain-rate-dependency characterisation of various nanocomposites as well as their impact performance.

First, a consistent manufacturing procedure is developed to manufacture all the material groups, namely FS, HNT, FS & HNT, Albipox 1000, Nanopox F700 and Albipox 1000 & Nanopox F700. Reinforced epoxy control samples with unreinforced epoxy are used for comparison to show the effects of the inclusions. The manufactured samples are put through experimental procedures including SEM, three-point bend tests under three different strain rates and Charpy impact tests. SEM images suggest that no significant material flaws exist in the manufactured samples. Also, the results of three-point bend show that the materials tends to be stiffer and more brittle under greater strain rates. Except for the rubber inclusions, which weaken and soften the material, all reinforcements increase the strength and stiffness of the composite materials. Other than HNT, all the inclusions lead to more ductile behaviour. In terms of impact performance, the material performances are evaluated based on two main groups: the first group consists of

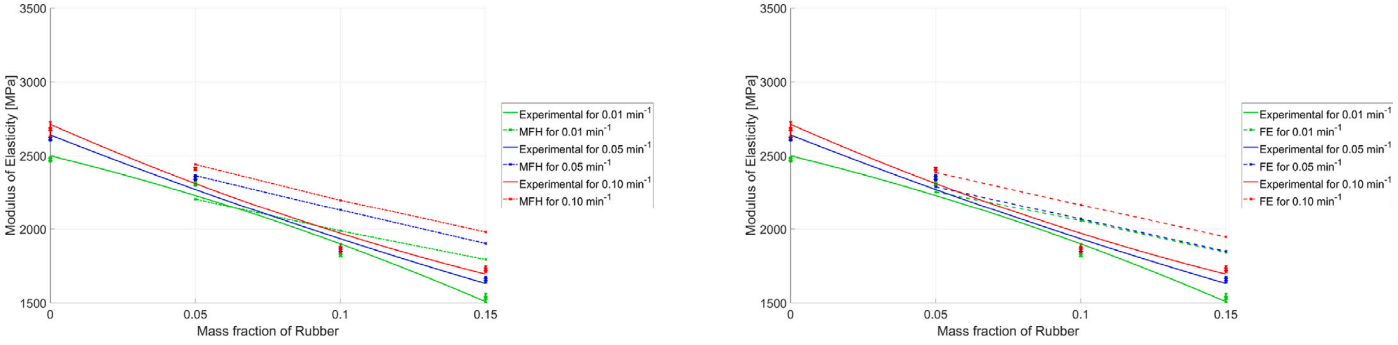

(a) Experimental versus MFH. (b) Experimental versus FE

Fig. 26. Comparison of experimental results for modulus of elasticity with the numerical simulations of rubber added epoxy.

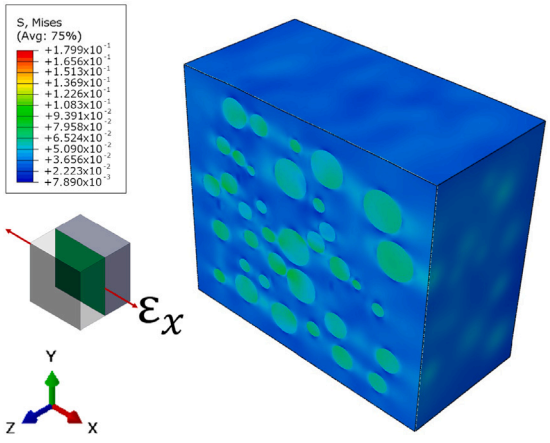

Fig. 27. A section view of an RVE with spherical silica inclusions with an average diameter of 20 nm taken between 5 – 50 nm (Stress unit: GPa).

FS and/or HNT reinforced epoxy, and the second group formed by silica and/or rubber reinforced epoxy. For the first group, the results show that FS is the most successful reinforcement when it comes to toughening. The addition of more FS, contributes more to the impact performance of the composite material. Whereas HNT has a completely different behaviour. The presence of HNT in the smallest amount increases the toughness but more addition of HNT may not always help. The combination of FS and HNT in equal masses exhibits a different behaviour than the previous two groups. The presence of HNT and FS in small amounts contributes significantly to the toughness, which is explained with the synergistic effects. However, adding more HNT and FS contributes little. In the second main group, where Evonik composites are, the materials show a more linear regarding the RC content and impact performance. Silica reinforcement toughens the composite material more than the rubber, and their equal mass mixture lies in between. Following the experimental studies, numerical simulations are performed employing MFH and FE methods. First, initial MFH simulations are run to determine the effective mechanical properties of the inclusions based on the experimental results. Then, using those determined mechanical properties, the effective mechanical properties of the composites are calculated and compared to the experimental results. Though the FE results tend to deliver a more accurate representation compared to the MFH results. Overall, the addition of FS offers the optimal mechanical behaviour with respect to maximum stresses that could be withstood. Also, the addition of both FS and HNT has a synergistic effect in not only optimising the maximum stress before breakage but also the impact energies. Overall, the results are in good agreement, and the stress analyses can reasonably explain the mechanical behaviour of these nanocomposite materials.

Finally, it is concluded that using multiple types of inclusions, with different mechanical characteristics, can be helpful in designing with filled epoxy composite materials due to synergistic effects.

CRediT authorship contribution statement

Mertol Tüfekci: Methodology, Formal analysis, Writing – original draft. **Burak Özkal:** Writing – review & editing. **Chris Maharaj:** Writing – review & editing. **Haibao Liu:** Methodology, Writing – review & editing. **John P. Dear:** Methodology, Writing – review & editing, Supervision. **Loïc Salles:** Writing – review & editing.

Declaration of competing interest

The authors declare that they have no known competing financial interests or personal relationships that could have appeared to influence the work reported in this paper.

Data availability

Data will be made available on request.

Acknowledgements

Mertol Tüfekci would like to acknowledge the support of the Scientific and Technological Research Council of Turkey (TUBITAK) (fund BİDEB 2213 2016/2) that makes this research possible.

The authors would like to thank Evonik for the courtesy of providing materials and Dr.Dr.-Ing. Stephan Sprenger for his helpful guidance.

The authors would also like to acknowledge computational resources and support provided by the Imperial College Research Computing Service (http://dx.doi.org/10.14469/hpc/2232).

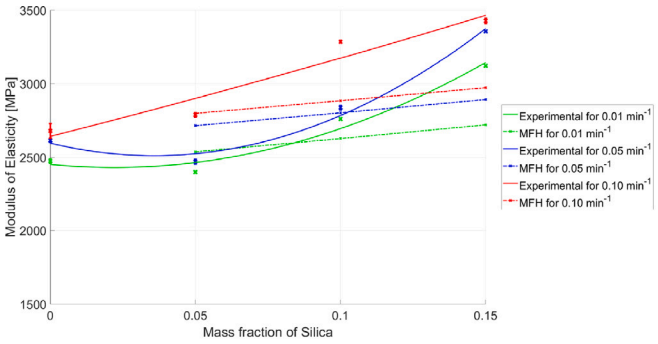

(a) Experimental versus MFH. (b) Experimental versus FE

Fig. 28. Comparison of experimental results for modulus of elasticity with the numerical simulations of silica reinforced epoxy.

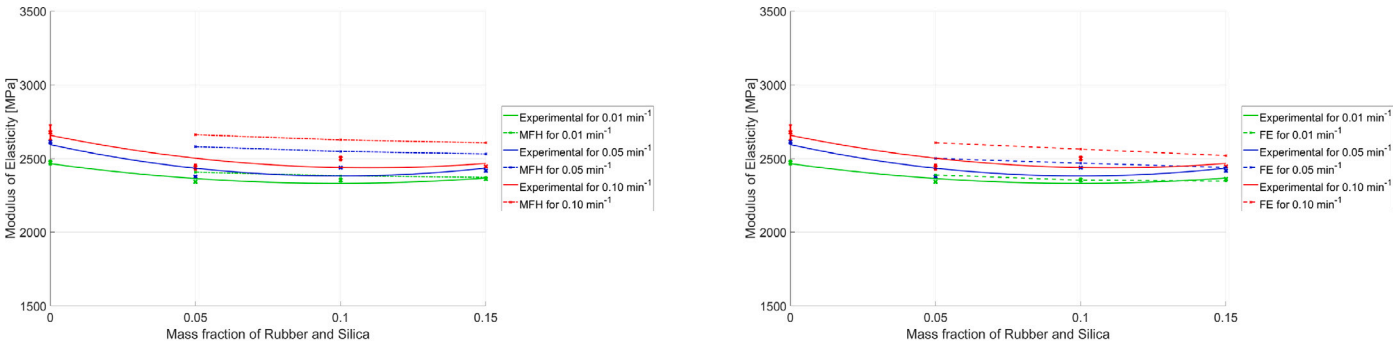

(a) Experimental versus MFH. (b) Experimental versus FE

Fig. 29. Comparison of experimental results for modulus of elasticity with the numerical simulations of silica and rubber reinforced epoxy.

References

[1] L. Brassart, I. Doghri, L. Delannay, Homogenization of elasto-plastic composites coupled with a nonlinear finite element analysis of the equivalent inclusion problem, Int. J. Solids Struct. 47 (5) (2010) 716–729, http://dx.doi.org/10.1016/j.ijsolstr.2009.11.013.

[2] H. Jrad, J.L. Dion, F. Renaud, I. Tawfiq, M. Haddar, Experimental characterization, modeling and parametric identification of the non linear dynamic behavior of viscoelastic components, Eur. J. Mech. A Solids 42 (2013) 176–187, http://dx.doi.org/10.1016/j.euromechsol.2013.05.004.

[3] S. Acarer, İ. Pir, M. Tüfekci, G. Türkoğlu Demirkol, N. Tüfekci, Manufacturing and characterisation of polymeric membranes for water treatment and numerical investigation of mechanics of nanocomposite membranes, Polymers 13 (10) (2021) http://dx.doi.org/10.3390/polym13101661, URL: https://www.mdpi.com/2073-4360/13/10/1661.

[4] I. Monetto, W.J. Drugan, A micromechanics-based nonlocal constitutive equation for elastic composites containing randomly oriented spheroidal heterogeneities, J. Mech. Phys. Solids 52 (2) (2004) 359–393, http://dx.doi.org/10.1016/S0022-5096(03)00103-0.

[5] W.J. Drugan, Two exact micromechanics-based nonlocal constitutive equations for random linear elastic composite materials, J. Mech. Phys. Solids 51 (9) (2003) 1745–1772, http://dx.doi.org/10.1016/S0022-5096(03)00049-8.

[6] J.J. Luo, I.M. Daniel, Characterization and modeling of mechanical behavior of polymer/clay nanocomposites, Compos. Sci. Technol. 63 (11) (2003) 1607–1616, http://dx.doi.org/10.1016/S0266-3538(03)00060-5.

[7] R.A. Schapery, On the characterization of nonlinear viscoelastic materials, Polym. Eng. Sci. 9 (4) (1969) 295–310, http://dx.doi.org/10.1002/pen.760090410, URL: http://onlinelibrary.wiley.com/doi/10.1002/pen.760090410/abstract.

[8] R.A. Schapery, Nonlinear viscoelastic constitutive equations for composites based on work potentials, Appl. Mech. Rev. 47 (1994) s269–s275, http://dx.doi.org/10.1115/1.3124421.

[9] S.E. Zeltmann, B.R. Bharath Kumar, M. Doddamani, N. Gupta, Prediction of strain rate sensitivity of high density polyethylene using integral transform of dynamic mechanical analysis data, Polymer 101 (2016) 1–6, http://dx.doi.org/10.1016/j.polymer.2016.08.053.

[10] E.T. Thostenson, C. Li, T.W. Chou, Nanocomposites in context, Compos. Sci. Technol. 65 (2005) 491–516, http://dx.doi.org/10.1016/j.compscitech.2004.11.003.

[11] Y.G. Miao, H.Y. Liu, T. Suo, Y.W. Mai, F.Q. Xie, Y.L. Li, Effects of strain rate on mechanical properties of nanosilica/epoxy, Composites B 96 (2016) 119–124, http://dx.doi.org/10.1016/j.compositesb.2016.04.008.

[12] A. Rathi, S. Kundalwal, S. Singh, A. Kumar, Adhesive and viscoelastic response of MWCNT/ZrO2 hybrid epoxy nanocomposites, J. Mech. Mater. Struct. 16 (2021) 281–292, http://dx.doi.org/10.2140/jomms.2021.16.281, URL: https://msp.org/jomms/2021/16-3/p03.xhtml.

[13] J. Fuller, S. Mitchell, T. Pozegic, X. Wu, M. Longana, M. Wisnom, Experimental evaluation of hygrothermal effects on pseudo-ductile thin ply angle-ply carbon/epoxy laminates, Composites B 227 (2021) 109388, http://dx.doi.org/10.1016/J.COMPOSITESB.2021.109388.

[14] T. Mace, J. Taylor, C. Schwingshackl, Simplified low order composite laminate damping predictions via multi-layer homogenisation, Composites B 234 (2022) 109641, http://dx.doi.org/10.1016/j.compositesb.2022.109641.

[15] B. Kim, J. Choi, S. Yang, S. Yu, M. Cho, Multiscale modeling of interphase in crosslinked epoxy nanocomposites, Composites B 120 (2017) 128–142, http://dx.doi.org/10.1016/j.compositesb.2017.03.059.

[16] S. Hao, Z. Li, C. Yang, A.J. Marsden, I.A. Kinloch, R.J. Young, Interfacial energy dissipation in bio-inspired graphene nanocomposites, Compos. Sci. Technol. 219 (2022) 109216, http://dx.doi.org/10.1016/J.COMPSCITECH.2021.109216.

[17] X. Lu, F. Detrez, J. Yvonnet, J. Bai, Identification of elastic properties of interphase and interface in graphene-polymer nanocomposites by atomistic simulations, Compos. Sci. Technol. 213 (2021) http://dx.doi.org/10.1016/j.compscitech.2021.108943.

[18] M. Owais, J. Zhao, A. Imani, G. Wang, H. Zhang, Z. Zhang, Synergetic effect of hybrid fillers of boron nitride, graphene nanoplatelets, and short carbon fibers for enhanced thermal conductivity and electrical resistivity of epoxy nanocomposites, Composites A 117 (2019) 11–22, http://dx.doi.org/10.1016/j.compositesa.2018.11.006.

[19] M. Bashar, U. Sundararaj, P. Mertiny, Microstructure and mechanical properties of epoxy hybrid nanocomposites modified with acrylic tri-block-copolymer and layered-silicate nanoclay, Composites A 43 (2012) 945–954, http://dx.doi.org/10.1016/j.compositesa.2012.01.010.

[20] X. Jin, J. Xu, Y. Pan, H. Wang, B. Ma, F. Liu, X. Yan, C. Wu, H. Huang, H. Cheng, C. Hong, X. Zhang, Lightweight and multiscale needle quartz fiber felt reinforced siliconoxycarbide modified phenolic aerogel nanocomposite with enhanced mechanical, insulative and flame-resistant properties, Compos. Sci. Technol. 217 (2022) 109100, http://dx.doi.org/10.1016/J.COMPSCITECH.2021.109100.

[21] S. Fan, C. Gao, C. Duan, S. Zhang, P. Zhang, L. Yu, Z. Zhang, Geometry effect of copper nanoparticles and nanowires on polyetheretherketone-matrix nanocomposites: Thermal conductivity, dynamic mechanical properties and wear resistance, Compos. Sci. Technol. 219 (2022) 109224, http://dx.doi.org/10.1016/J.COMPSCITECH.2021.109224.

[22] M. Tüfekci, T. Mace, B. Özkal, J.P. Dear, C.W. Schwingshackl, L. Salles, Dynamic behaviour of a nanocomposite: Epoxy reinforced with fumed silica nanoparticles, in: XXV ICTAM, Milano, 2021.

[23] S. Sprenger, Nanosilica-toughened epoxy resins, Polymers 12 (8) (2020) http://dx.doi.org/10.3390/polym12081777.

[24] N.G. Ozdemir, T. Zhang, I. Aspin, F. Scarpa, H. Hadavinia, Y. Song, Toughening of carbon fibre reinforced polymer composites with rubber nanoparticles for advanced industrial applications, Express Polym. Lett. 10 (5) (2016) 394–407, http://dx.doi.org/10.3144/expresspolymlett.2016.37, URL: http://www.expresspolymlett.com/letolt.php?file=EPL-0006743&mi=c.

[25] M. Battistella, M. Cascione, B. Fiedler, M.H. Wichmann, M. Quaresimin, K. Schulte, Fracture behaviour of fumed silica/epoxy nanocomposites, Composites A 39 (2008) 1851–1858, http://dx.doi.org/10.1016/j.compositesa.2008.09.010.

[26] M. Zappalorto, A. Pontefisso, A. Fabrizi, M. Quaresimin, Mechanical behaviour of epoxy/silica nanocomposites: Experiments and modelling, Composites A 72 (2015) 58–64, http://dx.doi.org/10.1016/j.compositesa.2015.01.027.

[27] J. Jordan, K.I. Jacob, R. Tannenbaum, M.A. Sharaf, I. Jasiuk, Experimental trends in polymer nanocomposites - A review, Mater. Sci. Eng. A 393 (2005) 1–11, http://dx.doi.org/10.1016/j.msea.2004.09.044.

[28] M. Kliem, J. Høgsberg, J. Vanwalleghem, A. Filippatos, S. Hoschützky, E.R. Fotsing, C. Berggreen, Damping analysis of cylindrical composite structures with enhanced viscoelastic properties, Appl. Compos. Mater. 26 (1) (2019) 85–113, http://dx.doi.org/10.1007/s10443-018-9684-2.

[29] X. Xu, N. Gupta, Determining elastic modulus from dynamic mechanical analysis data: Reduction in experiments using adaptive surrogate modeling based transform, Polymer 157 (2018) 166–171, http://dx.doi.org/10.1016/j.polymer.2018.10.036.

[30] X. Xu, C. Koomson, M. Doddamani, R.K. Behera, N. Gupta, Extracting elastic modulus at different strain rates and temperatures from dynamic mechanical analysis data: A study on nanocomposites, Composites B 159 (2019) 346–354, http://dx.doi.org/10.1016/j.compositesb.2018.10.015.

[31] R. Esmaeeli, H. Aliniagerdroudbari, S.R. Hashemi, C. Jbr, S. Farhad, Designing a new dynamic mechanical analysis (DMA) system for testing viscoelastic materials at high frequencies, Model. Simul. Eng. 2019 (2019) http://dx.doi.org/10.1155/2019/7026267.

[32] E. Pierro, G. Carbone, A new technique for the characterization of viscoelastic materials: Theory, experiments and comparison with DMA, J. Sound Vib. 515 (2021) 116462, http://dx.doi.org/10.1016/j.jsv.2021.116462, URL: https://doi.org/10.1016/j.jsv.2021.1164.

[33] M. Zhou, J. Liu, H. Yang, L. Zhang, A multi-scale analysis on reinforcement origin of static and dynamic mechanics in graphene-elastomer nanocomposites, Compos. Sci. Technol. (2022) 109617, http://dx.doi.org/10.1016/J.COMPSCITECH.2022.109617, URL: https://linkinghub.elsevier.com/retrieve/pii/S0266353822003591.

[34] M. Tufekci, Q. Rendu, J. Yuan, J.P. Dear, L. Salles, A.V. Cherednichenko, Stress and modal analysis of a rotating blade and the effects of nonlocality, in: Proceedings of the ASME Turbo Expo, Vol. 10B-2020, American Society of Mechanical Engineers, 2020, pp. 1–12, http://dx.doi.org/10.1115/GT2020-14821, URL: https://asmedigitalcollection.asme.org/GT/proceedings/GT2020/84225/Virtual,Online/1095287.

[35] K. Bertoldi, D. Bigoni, W.J. Drugan, Structural interfaces in linear elasticity. Part I: Nonlocality and gradient approximations, J. Mech. Phys. Solids 55 (2007) 1–34, http://dx.doi.org/10.1016/j.jmps.2006.06.004.

[36] W.J. Drugan, J.R. Willis, A micromechanics-based nonlocal constitutive equation and estimates of representative volume element size for elastic composites, J. Mech. Phys. Solids 44 (1996) 497–524, http://dx.doi.org/10.1016/0022-5096(96)00007-5.

[37] M.K. Hassanzadeh-Aghdam, Evaluating the effective creep properties of graphene-reinforced polymer nanocomposites by a homogenization approach, Compos. Sci. Technol. 209 (2021) 108791, http://dx.doi.org/10.1016/J.COMPSCITECH.2021.108791.

[38] T. Mori, K. Tanaka, Average stress in matrix and average elastic energy of materials with misfitting inclusions, Acta Metall. 21 (5) (1973) 571–574, http://dx.doi.org/10.1016/0001-6160(73)90064-3.

[39] G.M. Odegard, T.C. Clancy, T.S. Gates, Modeling of the mechanical properties of nanoparticle/polymer composites, Polymer 46 (2) (2005) 553–562, http://dx.doi.org/10.1016/j.polymer.2004.11.022, arXiv:0444500847.

[40] M. Tüfekci, S.G. Durak, İ. Pir, T.O. Acar, G.T. Demirkol, N. Tüfekci, Manufacturing, characterisation and mechanical analysis of polyacrylonitrile membranes, Polymers 12 (10) (2020) 1–21, http://dx.doi.org/10.3390/polym12102378.

[41] M. Tüfekci, İ. Pir, E. Tüfekci, Nondimensional analysis of two-dimensional elastic porous materials with regularly distributed circular holes, in: XXV ICTAM, 2021.

[42] S.M. Mirkhalaf, E.H. Eggels, T.J. van Beurden, F. Larsson, M. Fagerström, A finite element based orientation averaging method for predicting elastic properties of short fiber reinforced composites, Composites B 202 (September) (2020) 108388, http://dx.doi.org/10.1016/j.compositesb.2020.108388.

[43] S. Krop, H.E. Meijer, L.C.V. Breemen, Multi-mode modeling of global and local deformation, and failure, in particle filled epoxy systems, Composites A 88 (2016) 1–9, http://dx.doi.org/10.1016/j.compositesa.2016.05.012.

[44] I. Guven, K. Cinar, Micromechanical modeling of particulate-filled composites using micro-CT to create representative volume elements, Int. J. Mech. Mater. Des. 15 (2019) 695–714, http://dx.doi.org/10.1007/s10999-018-09438-6.

[45] S. Bargmann, B. Klusemann, J. Markmann, J.E. Schnabel, K. Schneider, C. Soyarslan, J. Wilmers, Generation of 3D representative volume elements for heterogeneous materials: A review, Prog. Mater. Sci. 96 (2018) 322–384, http://dx.doi.org/10.1016/j.pmatsci.2018.02.003.

[46] S.D. Müzel, E.P. Bonhin, N.M. Guimarães, E.S. Guidi, Application of the finite element method in the analysis of composite materials: A review, Polymers 12 (4) (2020) http://dx.doi.org/10.3390/POLYM12040818.

[47] R. Berahman, M. Raiati, M. Mehrabi Mazidi, S.M.R. Paran, Preparation and characterization of vulcanized silicone rubber/halloysite nanotube nanocomposites: Effect of matrix hardness and HNT content, Mater. Des. 104 (2016) 333–345, http://dx.doi.org/10.1016/j.matdes.2016.04.099.

[48] G. Ravichandran, G. Rathnakar, N. Santhosh, R. Chennakeshava, M.A. Hashmi, Enhancement of mechanical properties of epoxy/halloysite nanotube (HNT) nanocomposites, SN Appl. Sci. 1 (4) (2019) 1–8, http://dx.doi.org/10.1007/s42452-019-0323-9.

[49] ASTM D7264/D7264M-07, Standard Test Method for Flexural Properties of Polymer Matrix Composite Materials, in: Annual Book of ASTM Standards, Vol. i, 2007, pp. 1–11, http://dx.doi.org/10.1520/D7264.

[50] H.M. Hsiao, I.M. Daniel, Strain rate behavior of composite materials, Composites B 29 (5) (1998) 521–533, http://dx.doi.org/10.1016/S1359-8368(98)00008-0.

[51] ASTM-D6110-10, Standard Test Method for Determining the Charpy Impact Resistance of Notched Specimens of Plastics, ASTM, 2010, p. 17, http://dx.doi.org/10.1520/D6110-18.1.

[52] A. Pontefisso, M. Zappalorto, M. Quaresimin, An efficient RVE formulation for the analysis of the elastic properties of spherical nanoparticle reinforced polymers, Comput. Mater. Sci. 96 (2015) 319–326, http://dx.doi.org/10.1016/j.commatsci.2014.09.030.

[53] I.V. Singh, A.S. Shedbale, B.K. Mishra, Material property evaluation of particle reinforced composites using finite element approach, J. Compos. Mater. 50 (2016) 2757–2771, http://dx.doi.org/10.1177/0021998315612539.

[54] R.V. Pucha, J. Worthy, Representative volume element-based design and analysis tools for composite materials with nanofillers, J. Compos. Mater. 48 (2014) 2117–2129, http://dx.doi.org/10.1177/0021998313494916.

[55] J.D. Fidelus, E. Wiesel, F.H. Gojny, K. Schulte, H.D. Wagner, Thermo-mechanical properties of randomly oriented carbon/epoxy nanocomposites, Composites A 36 (2005) 1555–1561, http://dx.doi.org/10.1016/j.compositesa.2005.02.006.

[56] I.M. Gitman, H. Askes, L.J. Sluys, Representative volume: Existence and size determination, Eng. Fract. Mech. 74 (2007) 2518–2534, http://dx.doi.org/10.1016/j.engfracmech.2006.12.021.

[57] G. Catalanotti, On the generation of RVE-based models of composites reinforced with long fibres or spherical particles, Compos. Struct. 138 (2016) 84–95, http://dx.doi.org/10.1016/j.compstruct.2015.11.039.

[58] D.J. Bray, P. Dittanet, F.J. Guild, A.J. Kinloch, K. Masania, R.A. Pearson, A.C. Taylor, The modelling of the toughening of epoxy polymers via silica nanoparticles: The effects of volume fraction and particle size, Polymer 54 (2013) 7022–7032, http://dx.doi.org/10.1016/j.polymer.2013.10.034.

[59] D. Carolan, A. Ivankovic, A.J. Kinloch, S. Sprenger, A.C. Taylor, Toughened carbon fibre-reinforced polymer composites with nanoparticle-modified epoxy matrices, J. Mater. Sci. 52 (2017) 1767–1788, http://dx.doi.org/10.1007/s10853-016-0468-5.

[60] T.H. Hsieh, A.J. Kinloch, K. Masania, A.C. Taylor, S. Sprenger, The mechanisms and mechanics of the toughening of epoxy polymers modified with silica nanoparticles, Polymer 51 (2010) 6284–6294, http://dx.doi.org/10.1016/j.polymer.2010.10.048.

[61] Y. Huang, A.J. Kinloch, Modelling of the toughening mechanisms in rubber-modified epoxy polymers - Part I Finite element analysis studies, J. Mater. Sci. 27 (10) (1992) 2753–2762, http://dx.doi.org/10.1007/BF00540702, URL: http://www.springerlink.com/index/10.1007/BF00540702.

[62] M. Abadyan, V. Khademi, R. Bagheri, P. Motamedi, M.A. Kouchakzadeh, H. Haddadpour, Loading rate-induced transition in toughening mechanism of rubber-modified epoxy, J. Macromol. Sci. B 49 (2010) 602–614, http://dx.doi.org/10.1080/00222341003595253.